Nonlinear energy harvesting based on a rotating system

Dan Wang[a,b]*, Fangqi Chen[a], Zhifeng Hao[b], Marian Wiercigroch[c]

[a] College of Aerospace Engineering, Nanjing University of Aeronautics and Astronautics, Nanjing 210016, China

[b] School of Mathematical Sciences, University of Jinan, Jinan 250022, China

[c] Centre for Applied Dynamics Research, University of Aberdeen, Scotland, United Kingdom

Abstract

A simple electromagnetic energy harvester with the cubic nonlinear stiffness is proposed, and the characteristics of dynamic responses as well as the potential power harvested are studied in this paper. The proposed nonlinear electromagnetic vibration energy harvester can be installed on the host base that is rotating at a constant speed and vibrating vertically. Considering the combination of the vertical vibrating and rotating frequency of the host base, the 1:1 primary resonance is investigated by the method of multiple scales. The dynamic characteristics of responses in terms of system parameters are studied and the bifurcation curves are constructed. In addition to possessing the resonance characteristics, some saddle-node bifurcations occur for the steady-state solutions under certain conditions. Moreover, the effects of system parameters on the output average power are investigated as well. The results of analysis show that multiple frequency bands and parameter regions are existed where the large power can be harvested due to the resonance condition and nonlinearity of the system. Introducing the nonlinearity not only can increase the value of the output power but also expand the frequency bands and parameter regions to harvest the large power. A carefully selected system parameters can help to optimize the average power harvesting in the design.

Keywords: nonlinear electromagnetic energy harvester, resonance, nonlinear responses, average power, multiple scale method

1 Introduction

Vibration Energy Harvesting (VEH) has been extensively researched in the past years due to its great potentials in reducing an environmental impact and stimulating development of autonomous devices, such as wireless sensors, wearable devices and monitoring devices for the structural health monitoring, medical implants [1, 2]. The vibrational energy harvesters convert vibrational energy from ambient environments to electrical energy, which in turn is converted into chemical energy in batteries and ultimately reducing carbon footprint and cost, and for devices installed in difficult to reach and (or) remote locations. However, there is one fundamental problem for classical linear vibration energy harvesters, which is effective frequency bandwidths [3] and limited the bandwidth only near the resonant frequencies, then limits their applications in typical wide frequency spectrum ambient environments. Some linear approaches have been used to increase the output power, like the anti-phase resonance method proposed in [4]. A generic schematic for energy flow in a VEH is shown in

*Corresponding author, Email: danwang2014518@hotmail.com

Fig.1, and it is clear that the efficiency is not only dependent of the effectiveness of energy conversion but equally on reduction of energy losses. In order to overcome the deficiency of linear energy harvesters as well as improve the efficiency for energy harvesting, some mechanisms were introduced to the mechanical part and electrical part respectively.

Specifically, for the mechanical system, the nonlinearity can appear through the restoring forces, the impact nonlinearities such as stopper techniques [5] and limiters [6] and parametric excitations [7–10]. In addition, increasing multiple resonances for the nonlinear system such as harmonic excitations [11, 12], noise-type excitations [13] have been applied to expand frequency bandwidths. For the electrical system, the nonlinearity can appear through elements such as diodes and designing multiple dynamic elements in nonlinear energy harvesters [14] and introducing the new materials to energy harvesting systems [15].

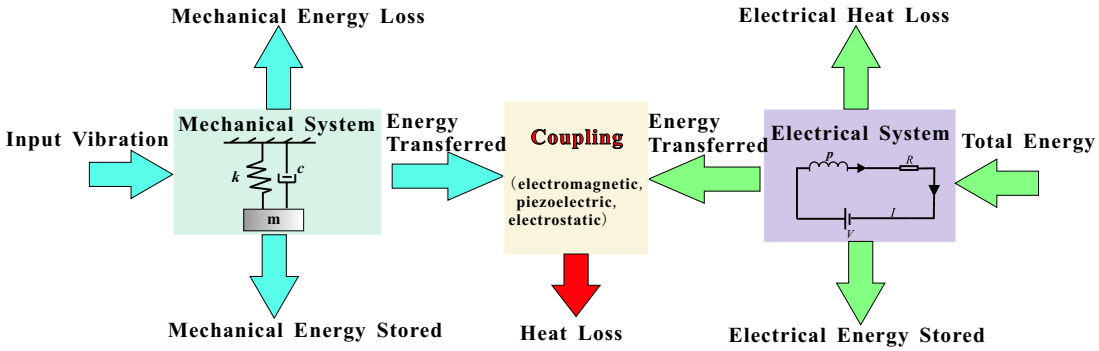

Figure 1: Schematic of energy flow in a typical Vibration Energy Harvester comprised of mechanical and electrical system and coupled via electromagnetic, electrostatic or piezoelectric mechanisms. Energy generation is accompanied with many loss sources in both systems and in between them, which need to be minimized to improve the overall efficiency.

The restoring forces for mechanical or magnetic spring or magnet are often expressed in the Duffing form[16–26], which can result in monostable, bistable and multi-stable systems and can be archetypes for energy harvesters. Bandwidths of monostable Duffing harvesters can broaden via the resonance effects, which are dependent on the strength of nonlinearity, damping as well as amplitude of responses. While the main difference between monostable and multi-stable energy harvesters is the characteristic of the nonlinear restoring force, that is, the nonlinear restoring force of the former has one stable static equilibrium position while the second has two or more stable static equilibrium positions (e.g. two or three stable static equilibrium positions). Some complex nonlinear restoring forces can be achieved through several linear springs or flexible beams geometrically connected, which include the tristable [27] or multi stable oscillations [28]. Specifically, Fig.2 shows an oscillator with a geometrically nonlinear stiffness [29, 30], which can be utilized in energy harvesters. As shown in Fig.2(a), two inclined springs were connected to the proof mass can provide the nonlinear stiffness. This idea can be practically realised by various beam harvesters shown in Fig.3. The nonlinear restoring force can have different origins in mechanics (a,b) [5] and magnetism (c,d) [31].

Furthermore, energy can be harvested from the rotating motion, which exists in all rotating machines [32, 33], wheels [34], shafts [35] and human motions [36, 37]. Three different types of energy harvesters based on the rotating motions were reported by Fu *et al.* [38], which include the inertial devices driven by the varying motion, continuously rotating devices using gravity as the counter force as well as fluid flow turbines.

The idea of energy harvesting from rotary motion can be related to extensive investigations on rotating pendular. The intrinsic nonlinearity of a rotating pendulum has been studied from both theoretical and applied perspectives extensively. Theoretical studies by Clifford and Bishop [39] showed rich dynamic behaviours such as rotational motions, equilibria, chaos and other complex responses.

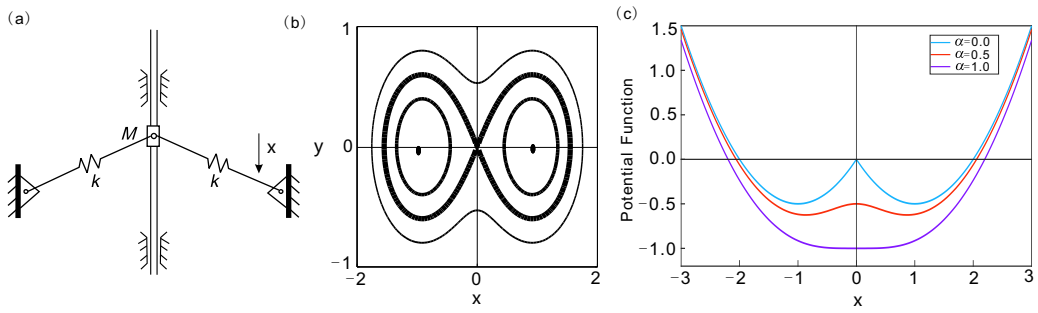

Figure 2: One of the simplest mechanical oscillator having a dual stability, which can be utilized for Vibration Energy Harvesting; (a) SD oscillator with strong geometrical nonlinearities, (b) and (c) phase portraits and potential energy showing the nature of dual stability [29, 30].

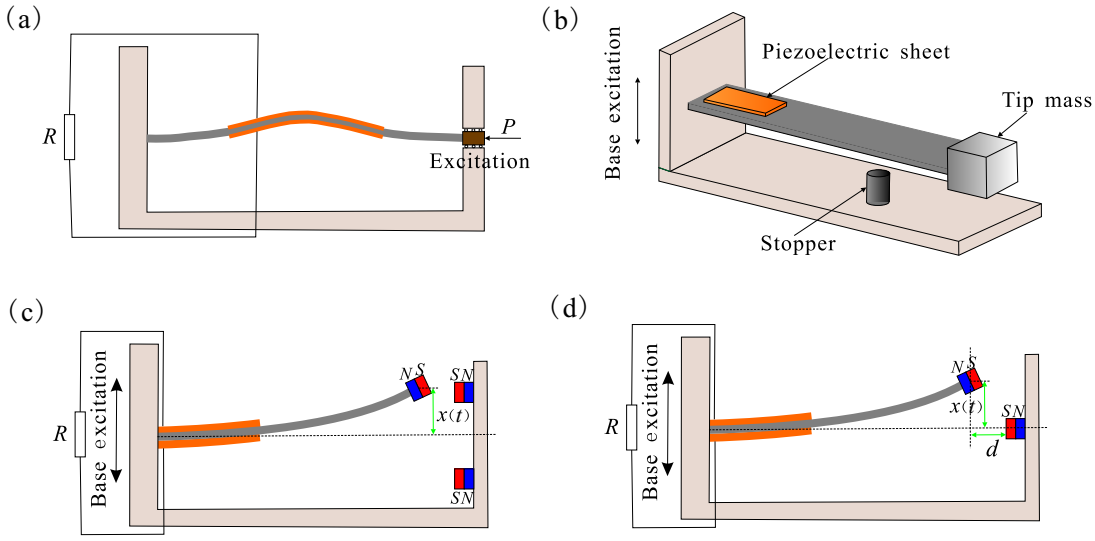

Figure 3: Examples of beam type of Vibration Energy Harvester; (a) bistable mechanical harvester, (b) mechanical harvester with one-side stopper [5], (c) and (d) magnetic harvesters [31].

These responses present a great potential for energy harvesting as has been pointed out by number of studies undertaken by the Centre for Applied Dynamics Research at the University of Aberdeen (see e.g. [40–42]), which can be seen as a wave-energy extraction device subjected to vertical base excitation from waves. The results presented in [40] revealed that the harvested power is strongly related with the period as well as type of the base excitation. In addition, a series of studies about the dynamics of the spring-pendulums and their possible applications[43, 44] in energy harvesting were carried out by the researchers. Specifically, Abohamer *et al.* [43] proposes a two-degree-of-freedom energy harvesting device whose archetype is the nonlinear damping spring pendulum that is supported by a point moving in a circular orbit. And Kecik [45] proposed a nonlinear system which can mitigate the simultaneous vibration and harvest energy from pendulum absorber.

The electromagnetic and piezoelectric devices which can harvest energy from the rotational systems have been investigated for various engineering applications [46–54], and the results reveal that nonlinear behaviors of energy harvesters yield a much wider operational frequency bandwidth.

For the rotating inertial harvesters, it is difficult to harvest energy from a rotating host motion with a constant speed, the rotating base's motion should vary in some way [38]. The linear electromagnetic and piezoelectric rotating energy harvesters with the base system vibrating were studied in [55]. The nonlinear energy harvesters in [56] were analysed by the load perturbation method, and the results showed that the high-energy oscillatory orbits can display both monostable and bistable systems. In

addition, the road profiles and roughness can be seen as sources of excitation to wheels' rotation [57]. Moreover, the centrifugal force due to the rotary motions can be seen as an excitation, which can be used for frequency tuning [58–60] or position adjusting [61]. Besides, the gyroscopic effect on a rotating piezoelectric device was considered in [62].

Moreover, some rotating energy harvesters were designed with consideration of the effect of Earth's gravity, which can be seen a varying excitation and therefore induce more resonant frequency bands. The rotating energy harvester which utilised the effect of gravity and proposed by Roundy and Tola [63] can present rich patterns of motions including the linear, monostable as well as bistable oscillations. By adjusting the gravity to the axial rotation, the piezoelectric energy harvesters [64, 65] can generate the power frequently.

Motivated by attractive characteristics of nonlinear vibration energy harvesters and a rotating mechanical system from the point of view of the base excitation (such as a load excitation on road wheels and the base excitation on the rotors or shafts), a generic nonlinear electromagnetic energy harvester is investigated in this paper with a view to exploit its complex dynamics for efficient energy harvesting.

The content of the paper is organized as follows. The mathematical model of the nonlinear energy harvester on a rotating base that vibrates in vertical direction is described in Section 2. Specifically, the governing equation is derived, the 1:1 primary resonance is investigated and the steady-state solutions of the system are obtained by using the multiple scale method. In Section 3, the effects of parameters on the responses of the free vibration are studied and the response curves are derived. Section 4 focuses on average output power from the nonlinear and linear systems. Then the paper is ended with conclusions drawn in Section 5.

2 Modelling and Methodology

In this section, the model of a single-degree of freedom electromagnetic energy harvester is constructed and the governing equation is derived. As an example of applications, the base system can be seen as a tire running on the road and the harvested energy can be used for the monitor system to collect data of the tire's motions. Then the multiple scale method is applied to analyse the possible resonance of the system.

2.1 Modelling of the nonlinear energy harvester

A proposed nonlinear energy harvesting device shown in Fig.4(a) is attached to a rotating base which has a constant angular velocity Ω and a radius r. At the same time, the base vibrates in the vertical direction periodically, $z(t) = Z\sin\omega t$. Here, the coordinate system in the plane that perpendicular to the axial direction are defined as the fixed inertial basis $\{\mathbf{i}, \mathbf{j}\}$ and the rotating basis $\{\mathbf{e_1}, \mathbf{e_2}\}$. The nonlinear energy harvesting device is shown in Fig.4(b), and consists of a small mass m, two horizontal springs fixed symmetrically between the moving mass and wall having stiffness k_h and a free length l, a vertical spring with the stiffness coefficient k_v, the structural damping c and the electromagnetic transfer part.

As shown in Fig.4(b) the electromagnetic harvesting device contains of a magnet fixed on the housing and two sets of coils connected to the moving mass. During the operation the current I will be generated when there is a relative motion between the magnet and coils. The deflection along the radial direction of the moving mass is assumed as $y(t)$ related to the host's vibration. The tangential vibration and the effects of gravity are not considered in this model. The generated voltage and force can be expressed as $V_e = \alpha\dot{y}$, $F_e = \alpha I$ according to the Ref. [20, 66], where α denotes the transduction factor. Moreover, according to the Kirchhoff's voltage law, the electromotive force acting on the moving mass can be rewritten in the following form after introducing the equivalent resistance R, that

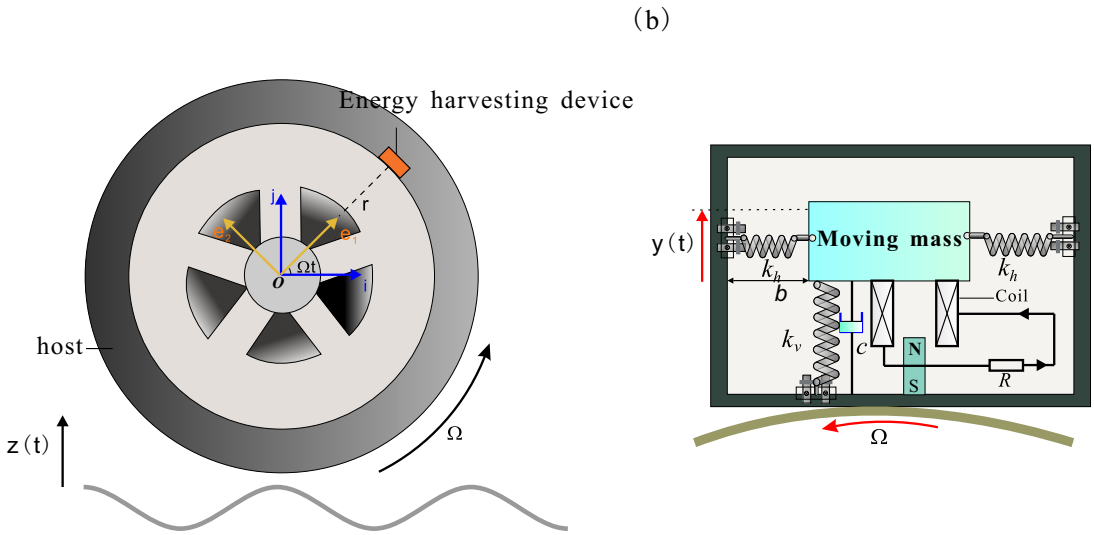

Figure 4: Schematic of a nonlinear energy harvester installed on a host system:(a) a host system rotating at the constant speed Ω and vibrating vertically as a harmonic oscillation; (b) the electromagnetic nonlinear energy harvester.

is,

$$F_e = \alpha I = \alpha \frac{V_e}{R} = \frac{\alpha^2}{R}\dot{y}. \tag{1}$$

The restoring force induced by the two horizonal and one vertical springs that effects on the mass in the radial direction can be expressed as follows,

$$F_h = k_v y(t) + 2k_h(\sqrt{y^2(t)+b^2} - l)\sin\beta, \tag{2}$$

where b denotes the horizontal distance between the fixed points of the mass and the horizontal spring, $\sin\beta = \dfrac{y(t)}{\sqrt{y^2(t)+b^2}}$. With assumption $y/b << 1$, the force then can be expanded as the following form including the nonlinear terms,

$$F_h \approx k_v y + 2k_h(1 - \frac{l}{b})y + \frac{k_h l}{b^3}y^3 + o(y^5). \tag{3}$$

Letting $k_1 = k_v + 2k_h(1-\dfrac{l}{b}), k_2 = \dfrac{k_h l}{b^3}$, the restoring force along the radial direction can be rewritten as $F_h = k_1 y + k_2 y^3$. The position and acceleration of the nonlinear energy harvesting device can be expressed as

$$\begin{aligned} \mathbf{r} &= (r+y)\mathbf{e_1} + z\mathbf{j}, \\ \ddot{\mathbf{r}} &= \ddot{y}\mathbf{e_1} + \ddot{z}\mathbf{j} - \Omega^2(r+y)\mathbf{e_1} + 2\Omega\dot{y}\mathbf{e_2}, \end{aligned} \tag{4}$$

where $\mathbf{j} = \sin\Omega t\mathbf{e_1} + \cos\Omega t\mathbf{e_2}$ that can be easily obtained by the coordinate transforming,

$$\begin{pmatrix} \mathbf{i} \\ \mathbf{j} \end{pmatrix} = \begin{bmatrix} \cos\Omega t & -\sin\Omega t \\ \sin\Omega t & \cos\Omega t \end{bmatrix} \begin{pmatrix} \mathbf{e_1} \\ \mathbf{e_2} \end{pmatrix}.$$

Along the direction of $\mathbf{e_1}$, the equation of the motion for the moving mass can be obtained as

$$m\ddot{y} + m\ddot{z}\sin\Omega t - m\Omega^2(r+y) = -c\dot{y} - F_e - (k_1 + k_2 y^2)y. \tag{5}$$

Substituting the electromotive force F_e and the excitation of the base $z(t)$ into Eq.(5), then the

equation of motion for the mass can be rewritten as

$$m\ddot{y} + \left(c + \frac{\alpha^2}{R}\right)\dot{y} + (k_1 - m\Omega^2)y + k_2 y^3 = mZ\omega^2 \sin\omega t \sin\Omega t + m\Omega^2 r. \tag{6}$$

Eq.(6) has two external forces acting on the energy harvesting system. One is the centripetal force and the other is related to the nondimensional rotating speed and the vibrating frequency of the host system, which becomes 0 when $\Omega t \approx 0, 2\pi \pmod{2\pi}$ and only has relation with the vibrating frequency ω when $\Omega t \approx \pi/2 \pmod{2\pi}$. Herein, the low-frequency rotating of the host is assumed and the rotating speed Ω satisfying that $k_1 > m\Omega^2$.

By introducing the nondimensional parameters

$$\omega_n = \sqrt{\frac{k_1}{m}},\ \tau = \omega_n t, y = Z\tilde{y}, \xi = \frac{c}{\omega_n m}, \eta = \frac{\alpha^2}{\omega_n m R}, \bar{\Omega} = \frac{\Omega}{\omega_n}, k = \frac{k_2 Z^2}{m\omega_n^2}, \bar{\omega} = \frac{\omega}{\omega_n}, \bar{r} = \frac{r}{Z},$$

Eq.(6) can be rewritten as

$$\ddot{\tilde{y}} + (\xi + \eta)\dot{\tilde{y}} + (1 - \bar{\Omega}^2)\tilde{y} + k\tilde{y}^3 = \frac{1}{2}\bar{\omega}^2[\cos(\bar{\Omega} - \bar{\omega})\tau - \cos(\bar{\Omega} + \bar{\omega})\tau] + \bar{\Omega}^2\bar{r}, \tag{7}$$

where ω_n denotes the natural frequency for the energy harvesting device, ξ is the nondimensional damping coefficient, η is the nondimensional coupling parameter for the electricalmechanic device, k is the nondimensional cubic nonlinear stiffness, $\bar{\Omega}$ and $\bar{\omega}$ are the nondimensional rotating speed and external frequency, $\bar{r}$ is the nondimensional radius. And $|\bar{\Omega} - \bar{\omega}|$, $\bar{\Omega} + \bar{\omega}$ denote the combined frequencies respectively.

2.2 Analysis on the 1:1 resonance using the multiple scale method

Due to the nonlinearity and excitation of dual forces, several resonances for the system can occur under certain parameter conditions. The research presented in [43, 67, 68] showed that the nonlinear systems could display rich dynamics under the resonance conditions, including the primary, superharmonic/subharmonic resonance as well as the internal resonances. Therefore, the multiple scale method[69–71] is applied to study the possible resonances for the system, which can help to understand some mechanisms about improving the energy harvesting efficiency of the system.

By introducing the scaling parameters as $\xi \to \varepsilon\xi$, $\eta \to \varepsilon\eta$, $k \to \varepsilon k$, one can obtain that

$$\ddot{\tilde{y}} + (1 - \bar{\Omega}^2)\tilde{y} = \frac{1}{2}\bar{\omega}^2[\cos(\bar{\Omega} - \bar{\omega})\tau - \cos(\bar{\Omega} + \bar{\omega})\tau] + \bar{\Omega}^2\bar{r} - \varepsilon(\xi + \eta)\dot{\tilde{y}} - \varepsilon k\tilde{y}^3. \tag{8}$$

Assume the approximate form of the solutions as follows,

$$\tilde{y}(t) = y_0(T_0, T_1) + \varepsilon y_1(T_0, T_1) + \cdots. \tag{9}$$

Substitute expression (9) into Eq. (8) and equate the coefficient of like powers of ε, then one can obtain that:

Order ε^0,

$$D_0^2 y_0 + (1 - \bar{\Omega}^2)y_0 = \frac{1}{2}\bar{\omega}^2[\cos(\bar{\Omega} - \bar{\omega})\tau - \cos(\bar{\Omega} + \bar{\omega})\tau] + \bar{\Omega}^2\bar{r}, \tag{10}$$

Order ε^1,

$$D_0^2 y_1 + (1 - \bar{\Omega}^2)y_1 = -(\xi + \eta)D_0 y_0 - k y_0^3 - 2D_0 D_1 y_0. \tag{11}$$

where $\frac{\mathrm{d}}{\mathrm{d}\tau} = D_0 + \varepsilon D_1 + \varepsilon^2 D_2$, $\frac{\mathrm{d}^2}{\mathrm{d}\tau^2} = D_0^2 + 2\varepsilon D_0 D_1$, and $D_n = \frac{\partial}{\partial T_n}$ is the partial differential operator.

The system (10) presents the forced vibration of the device under the excitation of the base's rotation and the centrifugal force, which corresponds to nonlinear system (7) for $k = 0$. The excitation frequencies can be $\pm(\bar{\Omega} - \bar{\omega})$ and $\bar{\Omega} + \bar{\omega}$. Due to the even characteristic of the excitation of the system, the analysis next will focus on the $(\bar{\Omega} - \bar{\omega})$ and $\bar{\Omega} + \bar{\omega}$ as the combined frequencies. Introducing $\omega_0 = \sqrt{1 - \bar{\Omega}^2}, \omega_1 = \bar{\Omega} - \bar{\omega}, \omega_2 = \bar{\Omega} + \bar{\omega}$ denote the natural frequency and the two combined frequencies of the nonlinear energy harvesting system. The solutions of Eq. (10) can be derived as

$$y_0 = \frac{Y_0}{2} + Y(T_1)e^{i\omega_0 T_0} + Y_1 e^{i\omega_1 T_0} + Y_2 e^{i\omega_2 T_0} + c.c., \tag{12}$$

where the first term on the right hand side denotes the response of the constant force and $Y_0 = \frac{\bar{\Omega}^2}{\omega_0^2}\bar{r}$, $Y_1 = \frac{\bar{\omega}^2}{4(\omega_0^2 - \omega_1^2)}$ and $Y_2 = \frac{\bar{\omega}^2}{4(\omega_2^2 - \omega_0^2)}$ respective denote the response amplitude under the external excitation, $Y(T_1)$ denotes the amplitude of the free vibration, and $c.c.$ stands for the complex conjugate of the proceeding terms.

Several possible resonances can occur due to the nonlinearities of the energy harvesting system, which are shown in Fig.5. Fig.5 indicates the possibilities of the primary resonances (e.g. $\omega_0 \approx \omega_{1,2}$), the superharmonic resonances (e.g. $\omega_0 \approx 2\omega_{1,2}$, $\omega_0 \approx 3\omega_{1,2}$) and the combined resonances (e.g. $\omega_0 \approx \omega_1 \pm \omega_2$, $\omega_0 \approx 2\omega_1 + \omega_2$, $\omega_0 \approx \omega_1 + 2\omega_2$), etc.

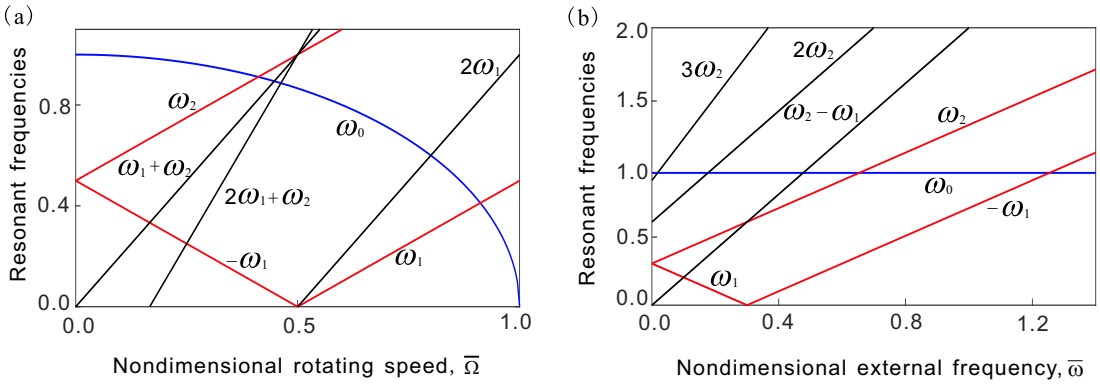

Figure 5: Possible resonant frequencies in terms of (a) the nondimensional rotating speed $\bar{\Omega}$ with $\bar{\omega}$ fixed at 0.5 and (b) nondimensional external frequency $\bar{\omega}$ with $\bar{\Omega}$ fixed at 0.3.

Herein the primary resonance $\omega_0 \approx \omega_1$ is studied in detail to investigate the effect of nonlinearity on the response and the average power of the nonlinear energy harvester. Letting $\omega_1 \approx \omega_0 + \varepsilon\sigma$, the solvable condition of Eq. (11) can be obtained when equating the coefficients of secular terms to be zero, reads

$$\begin{aligned} D_1 Y = {} & \frac{3k}{2\omega_0} i(\bar{Y}Y + Y_0^2 + 2Y_1^2 + 2Y_2^2)Y + \frac{3k}{2\omega_0} i(2Y\bar{Y}Y_1 + Y_0^2 Y_1 + Y_1^3 + 2Y_1 Y_2^2)e^{i\sigma T_1} \\ & + \frac{3k}{2\omega_0} i Y_1^2 \bar{Y} e^{2i\sigma T_1} + \frac{3k}{2\omega_0} i Y_1 Y^2 e^{-i\sigma T_1} - \frac{(\xi + \eta)}{2\omega_0}(\omega_0 Y + \omega_1 Y_1 e^{i\sigma T_1}), \end{aligned} \tag{13}$$

where $\bar{Y}$ denotes complex conjugate of Y. The functions Y can be expressed in the complex form as

$$Y = \frac{1}{2} a(T_1) e^{i\theta(T_1)}, \tag{14}$$

where a, θ respective denote the amplitude and phase angle. After substituting Eq.(14) into Eq.(13), the first-order differential equations can be obtained after separating the real and imaginary parts:

$$\begin{aligned} a' = &-\frac{(\xi+\eta)}{2}a + \frac{3k}{\omega_0}(\frac{a^2}{4}Y_1 + Y_0^2Y_1 + Y_1^3 + 2Y_1Y_2^2)\sin\phi \\ &+\frac{3k}{2\omega_0}Y_1^2 a\sin 2\phi - \frac{(\xi+\eta)}{\omega_0}\omega_1 Y_1\cos\phi, \end{aligned} \tag{15}$$

$$\begin{aligned} \phi' = &\frac{3k}{\omega_0}(\frac{a^2}{8} + (Y_1^2 + Y_2^2) + \frac{1}{2}Y_0^2) + \frac{3k}{a\omega_0}(\frac{3a^2}{4}Y_1 + Y_0^2Y_1 + Y_1^3 + 2Y_1Y_2^2)\cos\phi \\ &+\frac{3k}{2\omega_0}Y_1^2\cos 2\phi + \frac{(\xi+\eta)}{a\omega_0}\omega_1 Y_1\sin\phi - \sigma, \end{aligned} \tag{16}$$

where $(')$ denotes the derivatives with respect to T_1, and $\phi = \theta - \sigma T_1$.

3 Bifurcations and effects of system parameters on free vibration

The steady-state solutions for the free vibration under different parameter conditions of system (10) are calculated, and the stabilities are determined by the Routh-Hurwitz criterion. In order to analyse the effect of the nonlinearity on the free responses, the frequency-response curve for $k = 0$ is calculated for a comparison with other responses. Fig.6 shows the response curves with respect to the nondimensional rotating frequency $\bar{\Omega}$ for different values of the cubic nonlinear parameter $k = 0, 0.01, 0.1$ and 0.3 respectively. All other parameters are fixed at $\xi = 0.01, \eta = 0.01, \bar{r} = 1, \bar{\omega} = 0.5, \sigma = 0.1$. It can be seen from Fig.6 when $k = 0$, the nonlinear system degenerates to a simple form. The amplitude-frequency equation for this case can be obtained when letting $a' = 0$ and $\phi' = 0$ in Eqs (15) and (16) with $k = 0$, that is

$$[4\sigma^2 + (\xi+\eta)^2]\omega_0^2 a^2 - 4(\xi+\eta)^2\omega_1^2 Y_1^2 = 0. \tag{17}$$

When $k = 0$, the amplitude a increases very slowly as $\bar{\Omega}$ increases until near $\bar{\Omega} \approx 0.9114$, where the resonance occurs between the natural frequency ω_0 and the external frequency ω_1 of system (10). The resonant peak of the amplitude is very high but the bandwidth is very narrow. When $\bar{\Omega}$ exceeds the resonant frequency, the amplitude a declines rapidly as $\bar{\Omega}$ increasing to 1. This resonant phenomenon also occur when $k \neq 0$, but the difference is that the resonant bandwidth is wider than that for $k = 0$. Moreover, the value of amplitude a decreases as the parameter k increases for a constant rotating speed for $\bar{\Omega} \in (0.9114, 1)$.

When $k = 0.01$, the stable solution of amplitude a increases very slowly as $\bar{\Omega}$ increases at first until near to $\bar{\Omega} = 0.4114$ where the frequency $\omega_0 \approx \omega_2$. The amplitude a has two small peaks and one valley around $\bar{\Omega} = 0.4114$. And after the second small peak, the solution of amplitude a decreases as $\bar{\Omega}$ increases until to $\bar{\Omega} = 0.6$. After $\bar{\Omega} = 0.6$, the amplitude a increases as $\bar{\Omega}$ increases until encounters a saddle-node (SN) bifurcation at $\bar{\Omega} = 0.7835$, which indicates the occurrence of unstable solutions. Then the solution of amplitude a jumps to the higher branch of the solution which decreases as $\bar{\Omega}$ increases until to $\bar{\Omega} = 0.8570$. Afterwards the solution of amplitude a increases rapidly as $\bar{\Omega}$ increases until approaches the resonant frequency $\bar{\Omega} \approx 0.9114$. While the solution of amplitude a has an opposite varying trend as $\bar{\Omega}$ decreases from $\bar{\Omega} \approx 0.9114$ until encounters another saddle-node (SN) bifurcation at $\bar{\Omega} = 0.7492$. Then the solution jumps to the branch of lower value, which possesses the opposite varying trend as $\bar{\Omega}$ decreases comparing with that of when $\bar{\Omega}$ increases.

For $k = 0.1$, the solution of amplitude a grows very slowly as $\bar{\Omega}$ increases until reaches $\bar{\Omega} = 0.287$. Then the solution increases rapidly up to a SN bifurcation point at $\bar{\Omega} = 0.3544$, at which the solution of amplitude a jumps to the higher branch of the solution. Afterwards, the higher value decreases

quickly until up to a valley near $\bar{\Omega} \approx 0.4114$. Then the solution increases rapidly to another peak at $\bar{\Omega} = 0.5262$, and afterwards the solution decreases as $\bar{\Omega}$ increases until to $\bar{\Omega} = 0.7628$. After that, the solution increases rapidly as $\bar{\Omega}$ increases until to $\bar{\Omega} \approx 0.9114$. While the solution of amplitude a has an opposite trend as $\bar{\Omega}$ decreases until encounters the SN bifurcation at $\bar{\Omega} = 0.3004$, and then it jumps to the branch of small value which decreases slowly as $\bar{\Omega}$ decreases. Another SN bifurcation occurs at $\bar{\Omega} = 0.0268$, at which the solution jumps to the branch of large value once again, then the solution increases as $\bar{\Omega}$ decreases approaching to 0.

When increasing the value of k, the SN bifurcation disappears and the amplitude a becomes stable, like that for $k = 0.3$. As can be seen from Fig.6 that the solution of amplitude a decreases as $\bar{\Omega}$ increases until up to the minimum value around $\bar{\Omega} \approx 0.4114$. Afterwards, the solution reaches the peak near $\bar{\Omega} = 0.5256$. Then it decreases firstly and increases rapidly as $\bar{\Omega}$ increases to the resonant frequency $\bar{\Omega} \approx 0.9114$.

The results presented in Fig.6 indicate that introducing the cubic nonlinearity can broaden the resonant bandwidth, and the solution of the amplitude a is larger than that of for $k = 0$ in several parameter regions of $\bar{\Omega}$ which could affect the possible output power. Moreover, the coexisting of the multiple solutions is verified by the numerical method for the original system. As shown in Fig.6 that two stable responses of the original system coexist for $\bar{\Omega} = 0.765$ and $k = 0.01$. In the following analysis, the similar verifications are carried out as well.

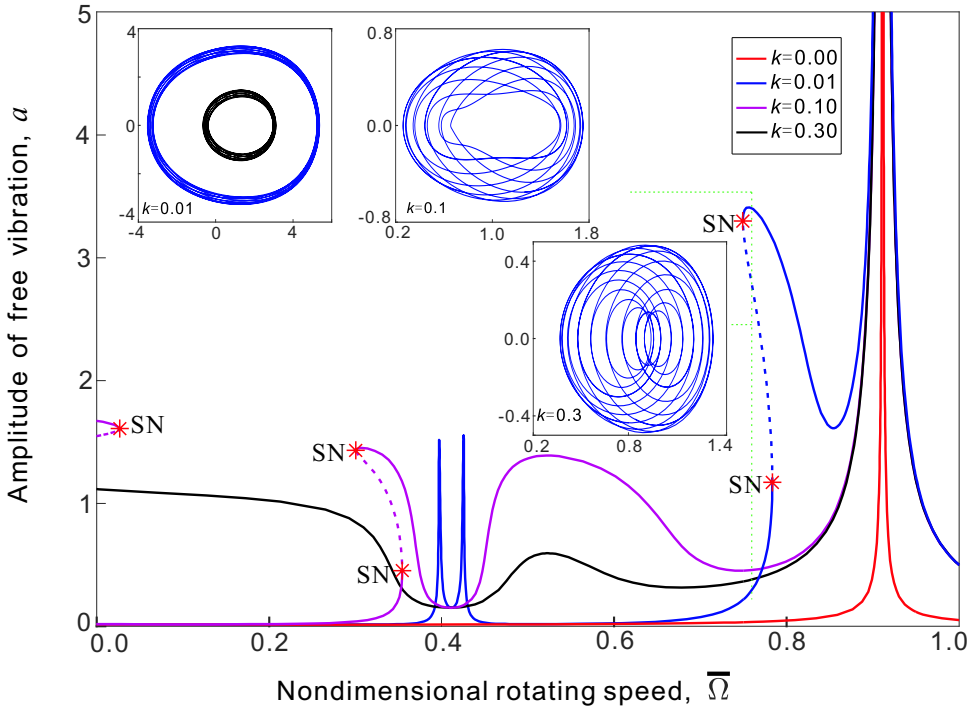

Figure 6: Response amplitude a versus the nondimensional rotating speed $\bar{\Omega}$ and representative phase portraits of the original system at $\bar{\Omega} = 0.765$ for different nonlinearities. The red curve denotes $k = 0$, blue curve denotes $k = 0.01$, violet curve denotes $k = 0.1$ and black curve denotes $k = 0.3$. The solid lines and dash lines denote the stable and unstable solutions, respectively. When $\bar{\Omega} = 0.765$, the phase portraits show two co-exiting stable solutions for $k = 0.01$ and one stable solution for $k = 0.1$ and $k = 0.3$ respectively.

The relations between the phase angle ϕ of the steady-state solution for the free vibration of system (10) and the nondimensional rotating speed $\bar{\Omega}$ are shown in Fig.7. For $k = 0$, the value of the phase angle ϕ is a constant value, reads 1.6705 when the nondimensional rotating speed $\bar{\Omega}$ is less than the resonant frequency 0.9114. While ϕ equals -1.4711 when $\bar{\Omega}$ exceeds the resonant frequency. This can be understood from Eq.(17) and the amplitude a can be expressed as

$$a = \pm \frac{2(\xi+\eta)\omega_1 Y_1}{\omega_0 \sqrt{4\sigma^2 + (\xi+\eta)^2}}. \tag{18}$$

Substituting the expression of a into the equations $a' = 0, \phi' = 0$, one can obtain that

$$\begin{aligned} \sin\phi &= \pm \frac{2\sigma}{\sqrt{4\sigma^2 + (\xi+\eta)^2}}, \\ \cos\phi &= \mp \frac{(\xi+\eta)}{\sqrt{4\sigma^2 + (\xi+\eta)^2}}. \end{aligned} \tag{19}$$

Expression (19) reveals that the phase angle ϕ is only related to parameters σ, ξ, η and is not dependent on the nondimensional frequencies $\bar{\Omega}, \bar{\omega}$ and nondimensional radius $\bar{r}$. And the specific constant value depends on the steady-state solutions that meet conditions $a' = 0$ and $\phi' = 0$.

Similarly, values of the phase angle ϕ will also jump from π to the very small value that near 0 when approaching to the resonant frequency $\bar{\Omega} \approx 0.9114$ for $k = 0.01, 0.1, 0.3$. Then the phase angle ϕ tends to the trivial solution as $\bar{\Omega}$ increases to 1. In addition, values of the phase angle ϕ would have two peaks near $\bar{\Omega} \approx 0.4114, 0.9114$ respectively for the parameter $k = 0.01, 0.1, 0.3$. While around $\bar{\Omega} \approx 0.5114$, the value of the phase angle ϕ reaches another small peak for $k = 0.01$ and it reaches the valleys for respective $k = 0.1, 0.3$. There would be SN bifurcations occurring as $\bar{\Omega}$ increases for $k = 0.01, 0.1$. Increasing the parameter k to 0.3, the solution of phase angle ϕ becomes stable.

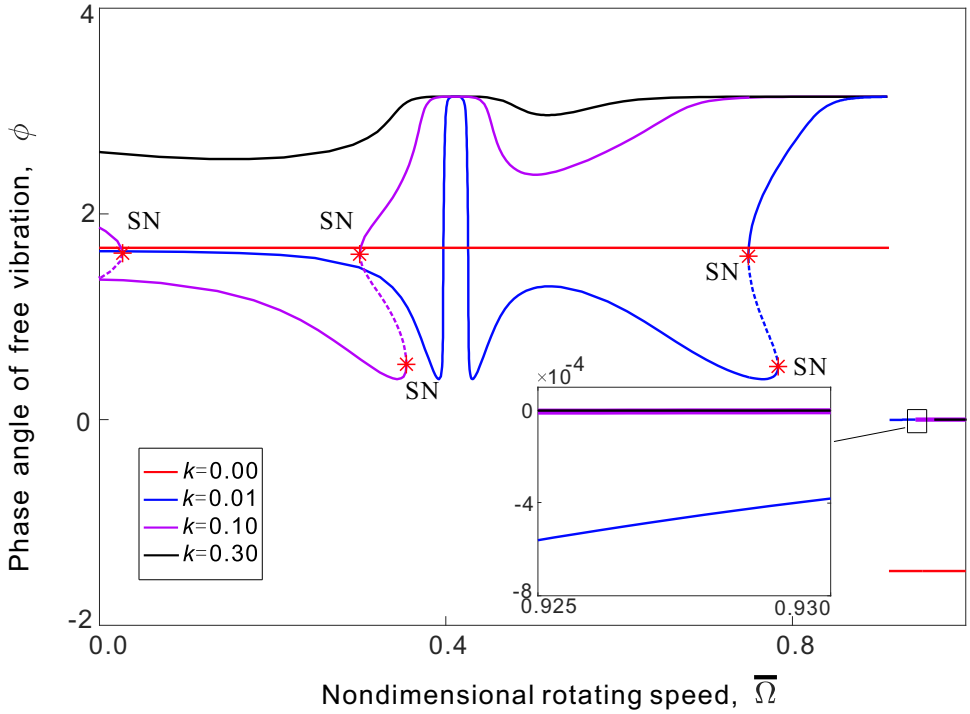

Figure 7: Phase angles ϕ versus the nondimensional rotating speed $\bar{\Omega}$. The red curve denotes $k = 0$, blue curve denotes $k = 0.01$, violet curve denotes $k = 0.1$ and black curve denotes $k = 0.3$. The solid lines and dash lines denote the stable and unstable solutions, respectively.

Fig.8 depicts the relations between the steady-state solutions of the amplitude a and phase angle ϕ with respect to the nondimensional frequency $\bar{\omega}$ for certain values of the nonlinear cubic parameter k. As a comparison, the solutions in terms of $\bar{\omega}$ are also studied for $k = 0$. The other parameters are fixed at $\xi = 0.01, \eta = 0.01, \bar{r} = 1, \sigma = 0.1, \bar{\Omega} = 0.3$.

As can be seen from Fig.8 that the response of amplitude a only has one resonant peak which occurs near $\bar{\omega} = 1.2539$ because one has that $\omega_0 \approx \bar{\omega} - \bar{\Omega}$. Meanwhile, the resonant bandwidth is wider for $k \neq 0$ than that for $k = 0$ and the bandwidth becomes narrow when increasing the value of k to some extent. For $k \neq 0$, the SN bifurcations occur under certain conditions. When $k = 0.01$, the solution of amplitude a increases as $\bar{\omega}$ increases until a SN bifurcation occurs at $\bar{\omega} = 0.6214$. Then the solution jumps to another branch of solution which decreases at first as $\bar{\omega}$ increases until up to the valley near $\bar{\omega} = 0.6539$. $\bar{\omega} = 0.6539$ is also an important point, because the natural frequency and the second external frequency satisfying $\omega_0 \approx \omega_2$ nearby. Afterwards, the solution goes up to a peak and another SN bifurcation occurs at $\bar{\omega} = 0.7005$. After that, it jumps to another branch of solution which decreases at first and then increases as $\bar{\omega}$ increases until encounters a SN bifurcation at $\bar{\omega} = 1.0760$. Then the solution of amplitude a jumps to a branch of solution of large value which increases rapidly as $\bar{\omega}$ increases until approaches to $\bar{\omega} = 1.2539$. While for $\bar{\omega}$ decreasing from certain value near $\bar{\omega} = 1.2539$, the solution of amplitude a decreases until a SN bifurcation occurs at $\bar{\omega} = 0.7972$, and then it jumps to a branch of small value solution which increases until encounters another bifurcation at $\bar{\omega} = 0.6947$. Afterwards, the solution jumps to another branch of solution which decreases at first and then increases until a SN bifurcation occurs at 0.6209 as $\bar{\omega}$ decreases. After that, it jumps to another branch of solution which tends to the trivial solution as $\bar{\omega}$ decreases to 0.

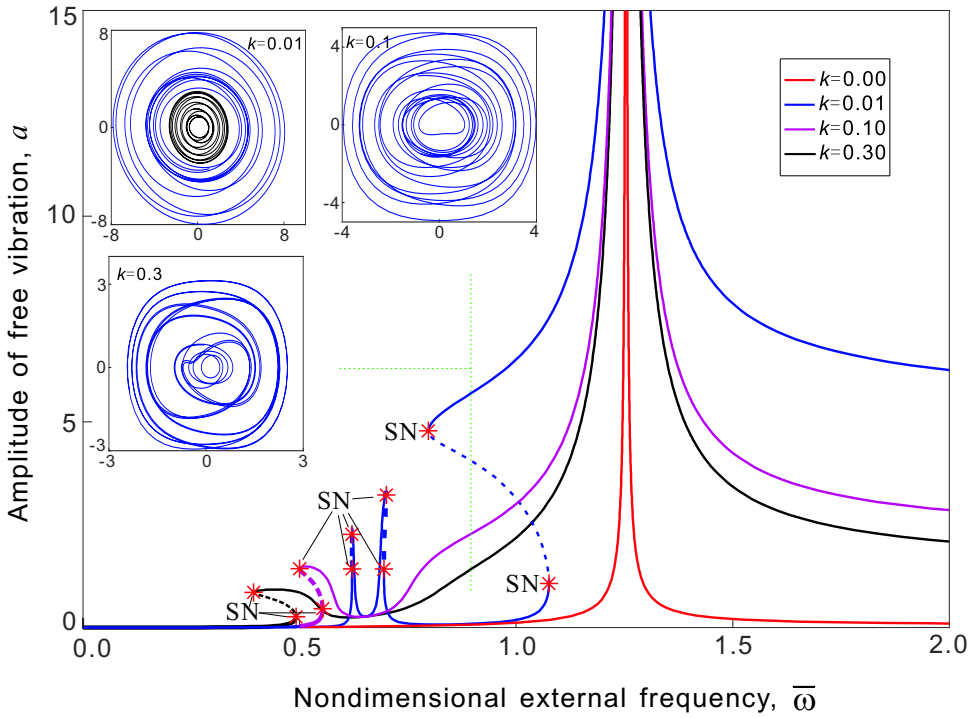

Figure 8: Amplitude a with respect to the nondimensional rotating speed $\bar{\omega}$ and phase portraits of the original system at $\bar{\omega} = 0.85$ for different strengths of nonlinearity. The red curve denotes $k = 0$, blue curve denotes $k = 0.01$, violet curve denotes $k = 0.1$ and black curve denotes $k = 0.3$. The solid lines and dash lines denote the stable and unstable solutions, respectively. When $\bar{\omega} = 0.85$, the phase portraits show two co-exiting stable solutions for $k = 0.01$ and one stable solution for $k = 0.1$ and $k = 0.3$ respectively.

For $k = 0.1$ and $k = 0.3$, a similar bifurcation characteristic occurs, such as the SN bifurcations. The solutions of amplitude a increase as $\bar{\omega}$ increases until encounter the SN bifurcations at $\bar{\omega} = 0.5535(k = 0.1), 0.4921(k = 0.3)$ respectively. Then the solutions jump to another branches of large value amplitudes. Afterwards, both of the solutions decrease at first until $\bar{\omega} \approx 0.6539$ and then increase rapidly to the resonant values respectively. While for $\bar{\omega}$ decreases from certain value less than 1.2, both solutions have the opposite varying trends comparing with that of for $\bar{\omega}$ increasing until

encounter the SN bifurcations at $\bar{\omega} = 0.5001(k = 0.1)$ and $0.3939(k = 0.3)$ respectively. Then the solutions jump to another branches of solutions and tend to the trivial solutions as $\bar{\omega}$ decreases to 0. However, the SN bifurcation occurs earlier for $k = 0.3$ than that for $k = 0.1$ as $\bar{\omega}$ varies and the value of amplitude a could become smaller when increasing the value of k at a constant nondimensional frequency $\bar{\omega}$. The comparison indicates that increasing the cubic nonlinearity effectively increases the stiffness of the system and suppresses the large-amplitude vibration.

As can be seen from Fig.9, for $k = 0$ the value of the phase angle ϕ is a constant and experiences a jump phenomenon when passing the resonant frequency. While for $k \neq 0$, the solutions of the phase angle ϕ posses two peaks which around π at $\bar{\omega} = 0.6539$ and 1.2539. When $\bar{\omega}$ exceeds the resonant frequency $\bar{\omega} = 1.2539$, the solutions of the phase angle ϕ jump to branches of small value and decrease as $\bar{\omega}$ increases. The varying trend of the phase angle ϕ for $k = 0.01$ changes dramatically in comparison to the other two situations for $k = 0.1, 0.3$. In addition, the solutions of phase angle ϕ experience the same SN bifurcations as that of the amplitude a for $k = 0.01, 0.1, 0.3$.

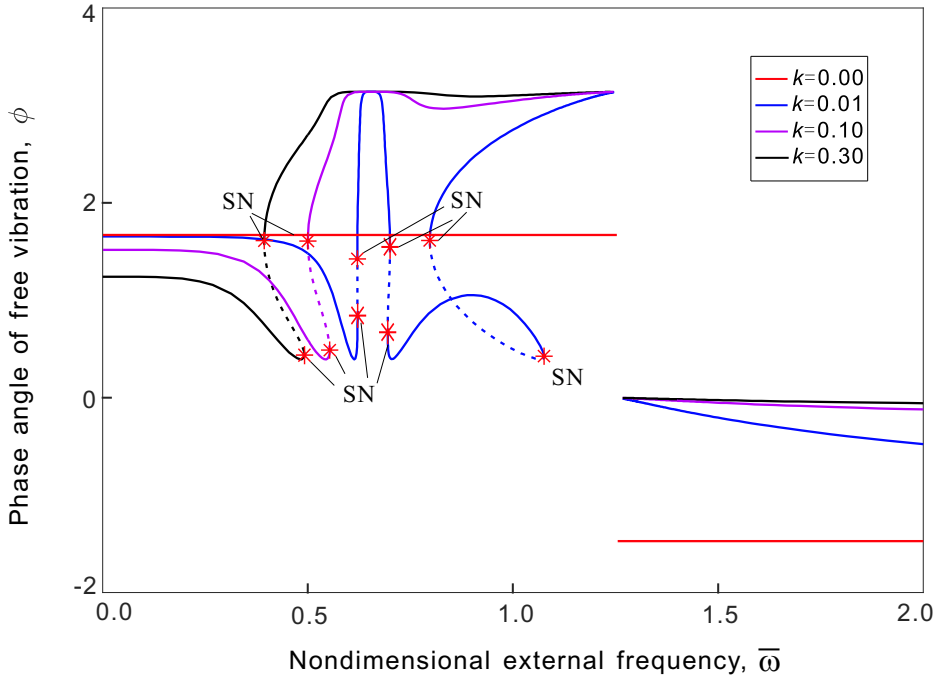

Figure 9: Curves of the phase angle ϕ versus the nondimensional rotating speed $\bar{\omega}$. The red curve denotes $k = 0$, blue curve denotes $k = 0.01$, violet curve denotes $k = 0.1$ and black curve denotes $k = 0.3$. The solid lines and dash lines denote the stable and unstable solutions, respectively.

Figs 10 and 11 show the relations of responses with respect to the parameter k under two different conditions, that is, the non-resonance and resonance with different parameter $\bar{\Omega}$. And the other parameters are fixed at $\xi = 0.01, \eta = 0.01, \bar{r} = 1, \sigma = 0.1, \bar{\omega} = 0.5$.

Fig.10 shows the varying trends of response curves in terms of the parameter k are similar for $\bar{\Omega} = 0.6$ and 0.75. While the SN bifurcations occur earlier for $\bar{\Omega} = 0.75$ than that of for $\bar{\Omega} = 0.6$, specifically, $k = 0.0162$ ($\bar{\Omega} = 0.75$) and $k = 0.0851$ ($\bar{\Omega} = 0.6$) for increasing the parameter k, $k = 0.0099$ ($\bar{\Omega} = 0.75$) and $k = 0.0401$ ($\bar{\Omega} = 0.6$)for decreasing the parameter k.

Fig.11 shows that the amplitude a would keep at the very high value when $\bar{\Omega}$ is selected near the resonance. There is a sharp drop for the amplitude a then it decreases slowly as k increases. Meanwhile, the value of the amplitude a would has the sharp drop when the $\bar{\Omega}$ stays away from the resonant frequency a little bit, such as $\bar{\Omega} = 0.915$. In addition, the varying trend of the phase angle ϕ is opposite to that of the amplitude a.

Fig.12 illustrates the response curves of the steady-state solutions of the amplitude a and the

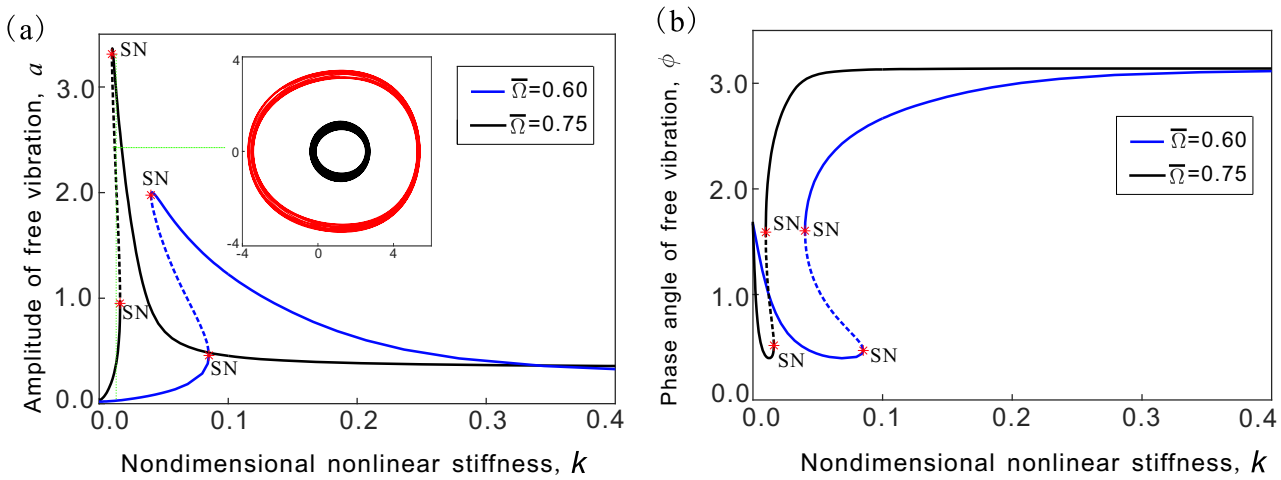

Figure 10: The response curves with respect to the cubic nonlinear parameter k far from the resonance condition: (a) amplitude a and phase portraits of the original system at $k = 0.01$; (b) phase ϕ. Blue curve denotes $\bar{\Omega} = 0.6$, black curve denotes $\bar{\Omega} = 0.75$. The solid lines and dash lines denote the stable and unstable solutions, respectively.

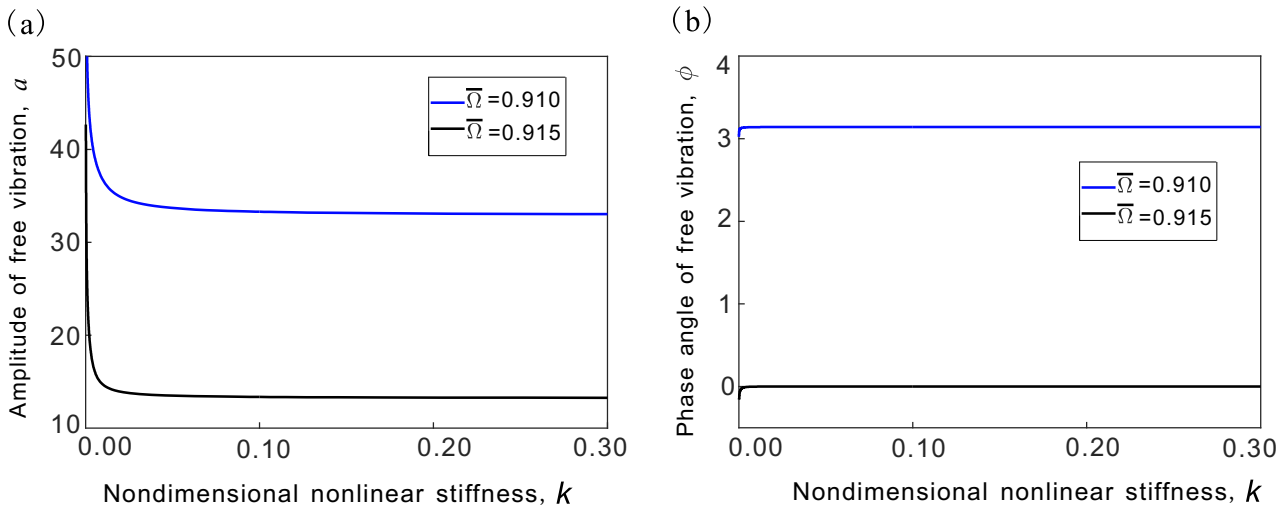

Figure 11: The response curves with respect to the cubic nonlinear parameter k near the resonance condition: (a) amplitude a; (b) phase ϕ. Blue curve denotes $\bar{\Omega} = 0.91$, black curve denotes $\bar{\Omega} = 0.915$.

phase angle ϕ with respect to the nondimensional radius $\bar{r}$ for different nonlinear conditions. The other parameters are fixed at $\xi = 0.01, \eta = 0.01, \sigma = 0.1, \bar{\Omega} = 0.75, \bar{\omega} = 0.5$. As can be seen from Fig.12(a) that the amplitude a and the phase angle ϕ are the constant values at $a = 0.0332, \phi = 1.6705$ for $k = 0$. There are two types of response curves for $k \neq 0$. One type is the stable solutions for $k = 0.1, 0.5$, where the responses of amplitude a decrease from the maximum value rapidly and then gradually as the nondimensional radius $\bar{r}$ increases. In contrast, the solutions of amplitude a increase as the nondimensional radius $\bar{r}$ increases until encounter the SN bifurcations at $\bar{r} = 2.0042(k = 0.005), 1.3395(k = 0.01)$. Then the solutions jump to the branches of high value solution, afterwards, the solutions decrease as the nondimensional radius $\bar{r}$ increases. Then the solutions of the amplitude a increase as the nondimensional radius $\bar{r}$ decreases until the SN bifurcations occur at $\bar{r} = 1.8993(k = 0.005), 0.9863(k = 0.01)$ respectively. After that, the solutions jump to the branches of small values which decrease as the nondimensional radius $\bar{r}$ decreases. The results indicate that increasing the nondimensional radius $\bar{r}$ could suppress the vibration of the system because the centrifugal force is strengthened.

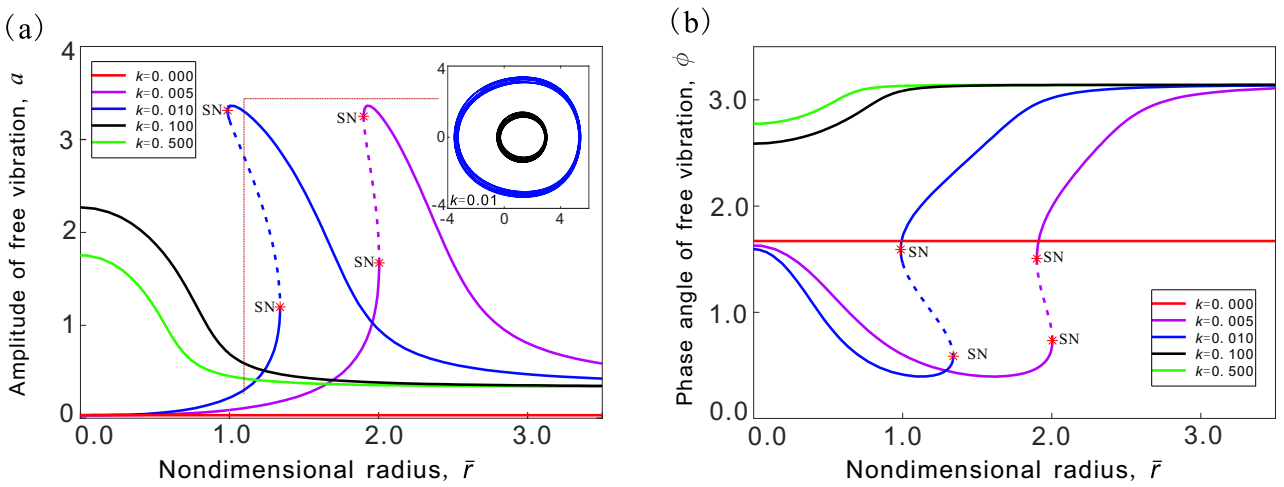

Figure 12: Response curves with respect to the nondimensional radius $\bar{r}$: (a) amplitude a and phase portraits of the original system at $\bar{r} = 1.1$; (b) phase ϕ. Red curve denotes $k = 0$, violet curve denotes $k = 0.005$, blue curve denotes $k = 0.01$, black curve denotes $k = 0.1$, green curve denotes $k = 0.5$. The solid lines and dash lines denote the stable and unstable solutions, respectively. Phase portrait shows two stable co-existing solutions for $\bar{r} = 1.1$ and $k = 0.01$.

Fig.12(b) shows that the varying trend of responses of the phase angle ϕ are opposite to that of the amplitude a when $k \neq 0$ and the solutions tend to the asymptotic value π as the nondimensional radius $\bar{r}$ increases.

Fig.13 presents the response curves for the amplitude a and the phase angle ϕ in terms of the detuning parameter σ for $k = 0, 0.01, 0.03$ respectively. The other parameters are fixed at $\xi = 0.01, \eta = 0.01, \bar{r} = 1, \bar{\Omega} = 0.75, \bar{\omega} = 0.5$, respectively. As can be seen from Fig.13(a) the amplitude is much larger for $k \neq 0$ than that for $k = 0$. There is a small peak around $\sigma = 0$ when $k = 0$. Increasing the value of k, the characteristics of the response curves have changes such as the occurring of the SN bifurcation. Specifically, for $k = 0.01$, the solution of the amplitude a increases as the detuning parameter σ is increasing until encounters a SN bifurcation at $\sigma = 0.0661$ where the solution jumps to a branch of small value solution. Then the solution decreases to the trivial solution as the detuning parameter σ increases. In contrast, when decreasing the detuning parameter σ from a certain condition, the solution decreases from a branch of high value until a SN bifurcation occurs at $\sigma = 0.0954$, where the solution jumps to a branch of small value. Afterwards, the solution increases as σ decreases until encounters the third SN bifurcation at $\sigma = 0.0583$, where the solution jumps to another branch. Then it decreases to the trivial solution as σ decreases. When $k = 0.03$, the solution of the amplitude a is stable and increases rapidly after $\sigma > 0$. However, at a constant detuning parameter, the value of the amplitude a is smaller for $k = 0.03$ than that of for $k = 0.01$. The result indicates that under the combination of resonances, system (10) and (11) can attain the large amplitude vibration in a wide parameter region, which is required for effective energy harvesting.

Fig.13(b) shows that for $k = 0$, the solution of the phase angle ϕ decreases slowly from 4.6803 as σ increases until near $\sigma = 0$ where the value of the phase angle ϕ decreases sharply to 1.7770. And then the solution decreases slowly as σ increases. For $k = 0.01$, the solution of the phase angle ϕ decreases as σ increases until encounters a SN bifurcation at $\sigma = 0.0661$ where the solution jumps to a branch of small value solution. Then it decreases gradually as σ increases. While decreasing σ from a certain value, the solution of the phase angle ϕ decreases as σ decreases until encounters another SN bifurcation at $\sigma = 0.0954$ where the solution jumps to a branch of small value. Then the solution increases as σ decreases until encounters the third SN bifurcation at $\sigma = 0.0583$ where the solution jumps to a branch of large value solution, after that it increases as σ increases. For $k = 0.03$, the solution of the phase angle ϕ is stable.

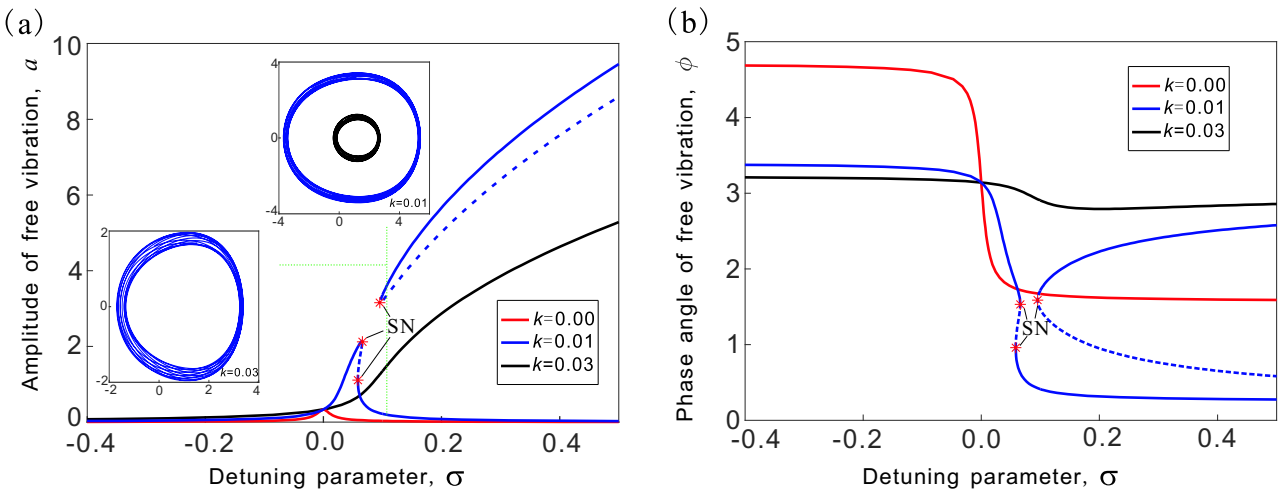

Figure 13: Response curves with respect to the detuning parameter σ: (a) the amplitude a and phase portraits of the original system for $k = 0.01$ (two stable solutions co-existing) and $k = 0.03$ (one stable solution) when $\sigma = 0.1$; (b) phase ϕ. Red curve denotes $k = 0$, blue curves denotes $k = 0.01$ and black curve denotes $k = 0.03$. The solid lines and dash lines denote the stable and unstable solutions, respectively.

The effects of the nondimensional coupling parameter η on the responses are shown in Fig.14. The other parameters are fixed at $\xi = 0.01, \bar{r} = 1, \sigma = 0.1, \bar{\Omega} = 0.75$ and $\bar{\omega} = 0.5$. As can be seen from Fig.14(a) that the amplitude a increases slowly as the parameter η increases when $k = 0$. While for $k = 0.01$, the values of amplitude a contains two branches and the SN bifurcation occurs. As η increases, the amplitude a increases slowly but the value is larger than that for $k = 0$. As η decreases, the amplitude a decreases until encounters a SN bifurcation at $\eta = 0.0102$ where the small solution jumps to a branch of large value solution, and then the large solution increases as η decreases. When enlarging the k to 0.1, the solution of the amplitude a is stable and is increasing gradually as η increases. Fig.14(b) illustrates that all the solutions are stable and are increasing gradually as η

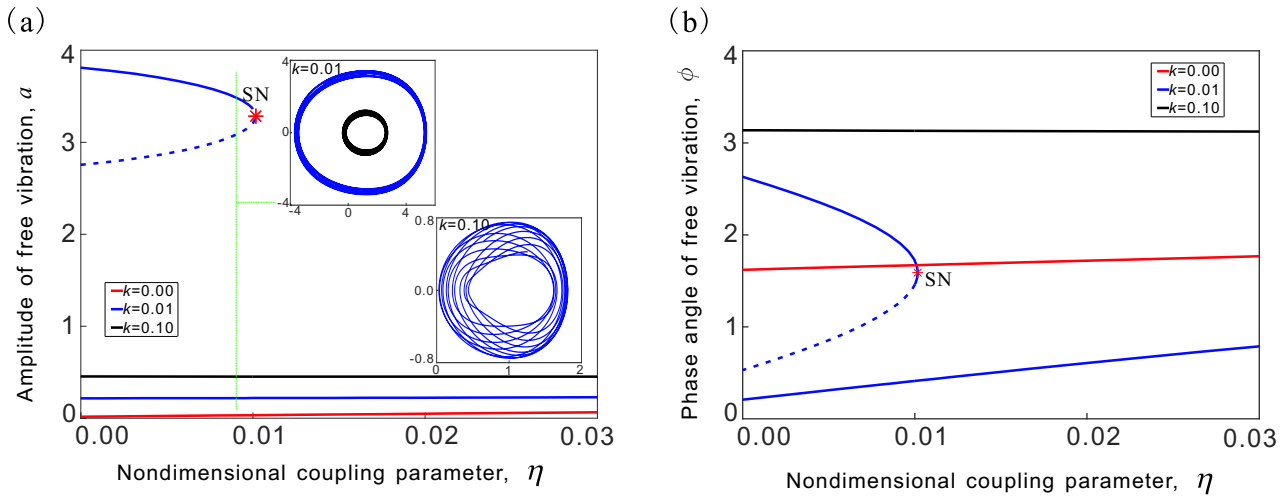

Figure 14: Response curves with respect to the nondimensional coupling parameter η: (a) amplitude a and phase portraits of the original system for $k = 0.01$ (two stable solutions co-existing) and $k = 0.1$ (one stable solution) when $\eta = 0.009$; (b) phase ϕ. Red curve denotes $k = 0$, blue curves denotes $k = 0.01$ and black curve denotes $k = 0.1$. The solid lines and dash lines denote the stable and unstable solutions, respectively.

increases for $k = 0, 0.01, 0.1$. While decreasing the parameter η, a SN bifurcation occurs resulting in the jump of the solution from the small branch to the large branch for $k = 0.01$.

Now, the first order asymptotic solution of the nonlinear system can be rewritten as

$$y_0 = Y_0 + a\cos(\omega_0 t + \theta) + 2Y_1\cos(\omega_1 t) + 2Y_2\cos(\omega_2 t), \tag{20}$$

where a and θ can be derived based on Eqs (15) and (16).

Without loss of generality, the asymptotic solutions (based on Eq.(20)) as well as the direct numerical solutions (based on Eq.(7)) are derived to further verify the analytical results. Some representative curves are shown in Fig.15, and it indicates that the analytical results have a good agreement with the numerical results.

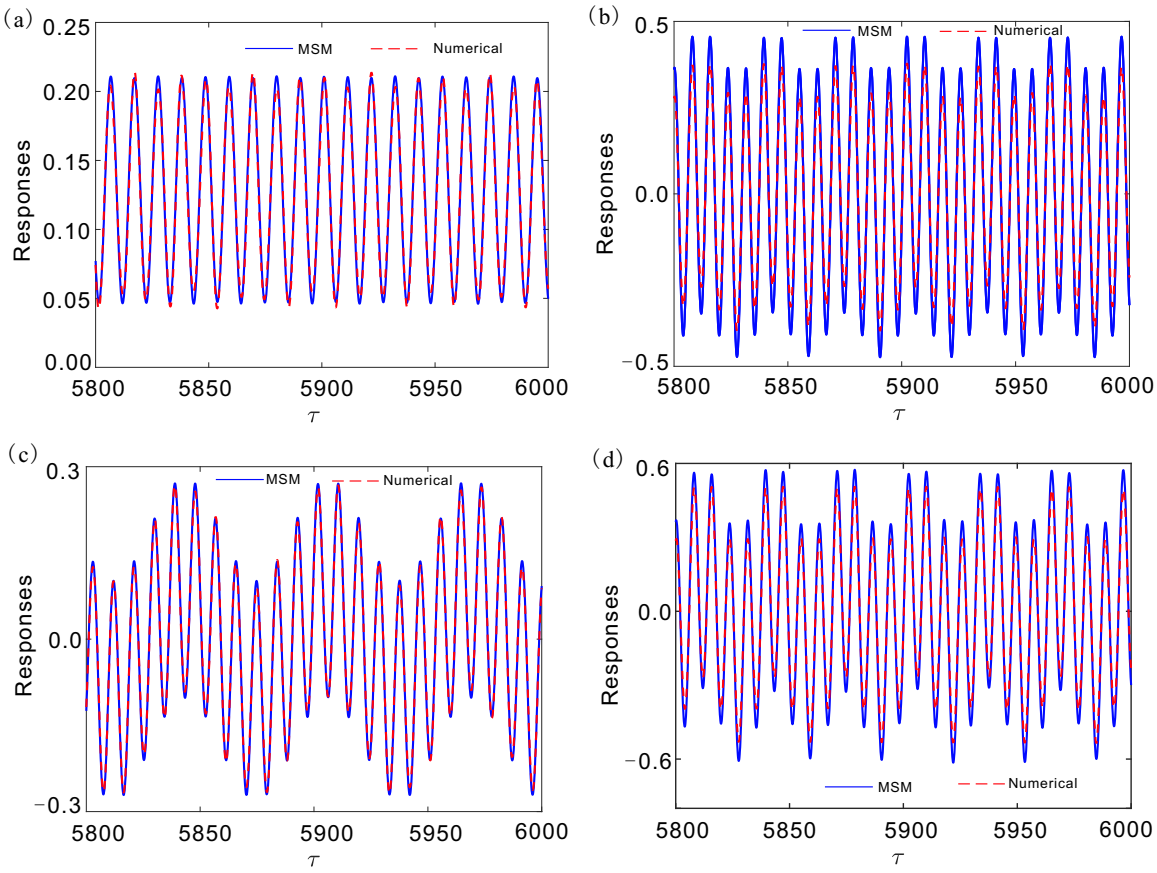

Figure 15: Time histories are obtained by the MSM and direction numerical simulation respectively. The system parameters are set as: (a) $\xi = 0.001, \eta = 0.001, \bar{\Omega} = 0.3, \bar{\omega} = 0.3, k = 0.3, \bar{r} = 0.8$; (b) $\xi = 0.001, \eta = 0.001, \bar{\Omega} = 0.5, \bar{\omega} = 0.3, k = 0.3, \bar{r} = 0$; (c) $\xi = 0.001, \eta = 0.001, \bar{\Omega} = 0.3, \bar{\omega} = 0.4, k = 0.3, \bar{r} = 0$; (d) $\xi = 0.001, \eta = 0.001, \bar{\Omega} = 0.3, \bar{\omega} = 0.5, k = 0.3, \bar{r} = 0.01$ respectively. The blue solid lines and red dash lines denote the asymptotic and direct numerical solutions, respectively.

4 Effects of system parameters on the average power output

In order to identify the optimal parameters for energy harvesting, effects of the system parameters on the average output power, especially the nonlinear parameter are investigated here. The nondimensional output power can be derived based on the first order solution (20) as $p = \eta\dot{y}_0^2$, which reads

that

$$
\begin{aligned}
p = \eta \dot{y}_0^2(t) = \frac{1}{2}\eta a^2\omega_0^2(1-\cos 2(\omega_0 t+\theta)) + 2Y_1^2\omega_1^2(1-\cos(2\omega_1 t))+ \\
2Y_2^2\omega_2^2(1-\cos(2\omega_2 t)) + 2a\omega_0 Y_1\omega_1(\cos(\omega_0 t-\omega_1 t+\theta)-\cos(\omega_0 t+\omega_1 t+\theta))+ \\
2a\omega_0 Y_2\omega_2(\cos(\omega_0 t-\omega_2 t+\theta)-\cos(\omega_0 t+\omega_2 t+\theta))+ \\
4Y_1 Y_2\omega_1\omega_2(\cos(\omega_2-\omega_1)t-\cos(\omega_1+\omega_2)t).
\end{aligned} \tag{21}
$$

Eq.(21) indicates that there are more frequency components contributing to the power output of the nonlinear energy harvester device, such as $2\omega_{0,1,2}, |\omega_0 - \omega_{1,2}|, \omega_0 + \omega_{1,2}, \omega_1 \pm \omega_2$.

Then the average harvested power over a period T can be calculated as $P = \frac{1}{T}\int_0^T pdt$. Substitute Eq.(21) into the integral formular, then expression can be rewritten as

$$
\begin{aligned}
P &= \frac{1}{2}\eta(a^2\omega_0^2 + 4Y_1^2\omega_1^2 + 4Y_2^2\omega_2^2) \\
&= \frac{1}{2}\eta\left(a^2\omega_0^2 + \frac{\omega_1^2\bar{\omega}^4}{(\omega_0^2-\omega_1^2)^2} + \frac{\omega_2^2\bar{\omega}^4}{(\omega_2^2-\omega_0^2)^2}\right).
\end{aligned} \tag{22}
$$

Eq.(22) indicates that the amplitude a for the free vibration of system (10) has the contribution to the average output power, which is the main difference between the nonlinear energy harvester studied in this paper and the linear energy harvester. And the average power from linear system can be easily obtained by letting $k = 0$, which only has the relations with the parameters $\eta, \bar{\Omega}, \bar{\omega}$. This is investigated to gain an insight on the relations between the average power and the parameters of the nonlinear energy harvester.

The curves of the average power P from linear and nonlinear energy harvester with respect to the nondimensional rotating speed $\bar{\Omega}$ computed for different nonlinearity are shown in Fig.16. And the other parameter are fixed at $\xi = 0.01, \eta = 0.01, \bar{r} = 1, \bar{\omega} = 0.5$. To make the comparison clearly, parts of the values for the average energy are chosen which not represent the maximum values during the resonant frequency bands.

The nonlinear energy harvesting system will degenerate to the linear system when $k = 0$. As can be seen from Fig.16 that there are two frequency bands with large values for the average power near the resonant frequencies $\bar{\Omega} = 0.4114, 0.9114$. And the frequency band near $\bar{\Omega} = 0.4114$ is wider than that near $\bar{\Omega} = 0.9114$, which has a good agreement with that of in the literature [55]. While for $k \neq 0$, the resonant frequency bands are still kept but some new characteristics appear like shown in Fig.16. When $k = 0.01$, a frequency band $[0.7484, 0.8523]$ for $\bar{\Omega}$ with a high average power (up to 0.0255) appears corresponding to the value from the linear system is very small. A similar varying trend occurs for $k = 0.04$ as that of for $k = 0.01$. However, one difference is that the frequency band $[0.6005, 0.6758]$ for $\bar{\Omega}$ with a high average power occurs earlier than that of for $k = 0.01$. And the other difference is that another two small frequency bands occur near the first resonant frequency, that is, $[0.3763, 0.3790]$, $[0.4437, 0.4477]$. Moreover, the relation curves varies as the nonlinearity parameter k increases.

As can be seen from Fig.16 that the varying trends of the average power versus the nondimensional rotating speed $\bar{\Omega}$ are similar for $k = 0.07$ to that of for $k = 0.1$. For example when $k = 0.1$, two frequency bands with higher average power appear because of the coexistence of the multiple solutions, that is, $\bar{\Omega} \in (0, 0.0266)$ and $\bar{\Omega} \in (0.3, 0.3525)$. And another wider frequency band $\bar{\Omega} \in (0.4696, 0.7)$ appears as well. The values of the average power of nonlinear system for $\bar{\Omega} \in (0, 0.0266)$ and $\bar{\Omega} \in (0.4696, 0.7)$ are much larger than their counterparts from the linear system.

Increasing the nondimensional nonlinear parameter again, the new characteristics exhibit, like the relation curves for $k = 0.2$ and $k = 0.3$ in Fig.16. For $k = 0.2$, a wider frequency band $\bar{\Omega} \in (0, 0.34)$ with the higher average power than its counterparts from linear system appears and the average power is a little higher than that of linear system when $\bar{\Omega} \in (0.48, 0.64)$. The results indicate that introducing

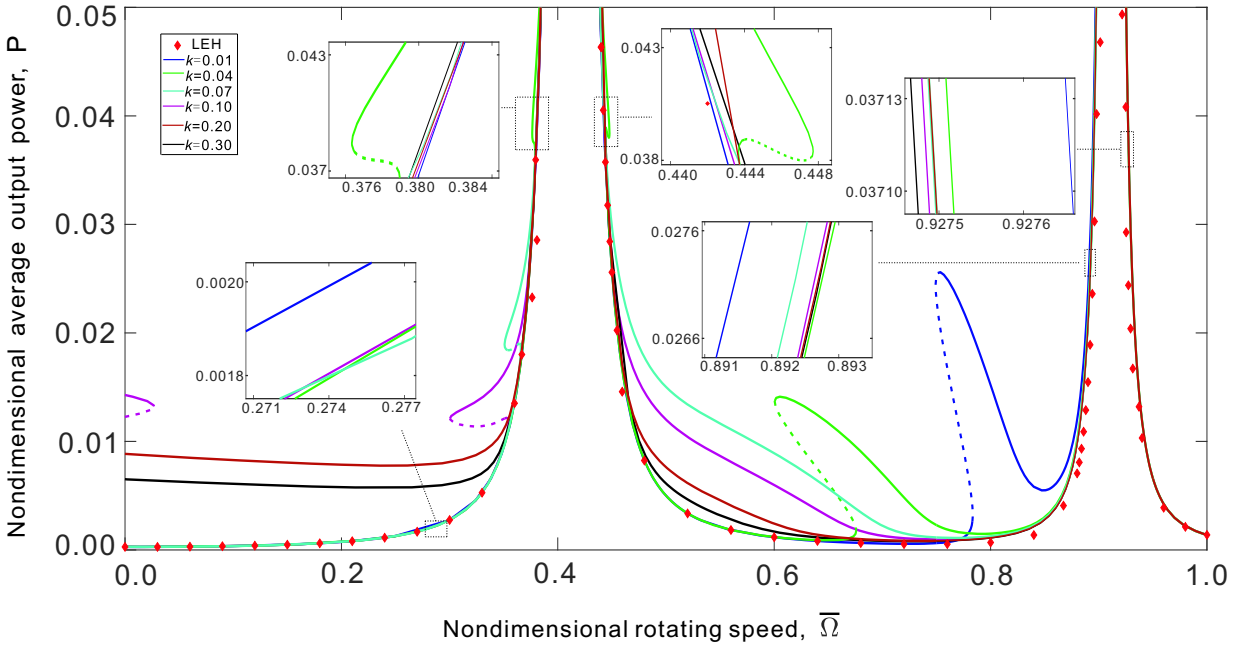

Figure 16: Relation curves of the nondimensional average output power P in terms of the nondimensional rotating speed $\bar{\Omega}$ with different cubic nonlinear parameters.

the nonlinearity could expand the bandwidth to harvest the large average power. Moreover, the new frequency band would appear in smaller nondimensional rotating frequency regions as the nonlinear parameter k increasing.

The relation curves of the average power from linear and nonlinear energy harvesting system with respect to the nondimensional external frequency $\bar{\omega}$ with different nonlinearities are shown in Fig.17. And the other parameters are fixed at $\xi = 0.01, \eta = 0.01, \bar{r} = 1, \bar{\Omega} = 0.3$, respectively. As can be seen from Fig.17 that when $k = 0$, the varying trend of average power versus the nondimensional external frequency $\bar{\omega}$ has a good agreement with that from the linear device. And the value of average power is very high in the two frequency bands near the resonant frequencies $\bar{\omega} = 0.6539, 1.2539$ and the band near $\bar{\omega} = 1.2539$ is about three times as that of near $\bar{\omega} = 0.6539$. However, in addition to maintain the linear characteristics, there some frequency bands with high values appear when $k \neq 0$ as can be seen from Fig.17. For $k = 0.01$, the bandwidth is expanded obviously near the second resonant frequency and the value of the power is much higher than its counterpart from $\bar{\omega} = 0.7972$ to $\bar{\omega} = 2$, especially, the high power is harvested when $\bar{\omega} \in (0.7972, 1.0708)$ because the coexistence of the multiple solutions. There is another small frequency band for $\bar{\omega} \in (0.6947, 0.7005)$ also has the high value for the coexisting of the multiple solutions. In addition, the relation curves between the average output power in terms of the nondimensional external frequency $\bar{\omega}$ varies as the nondimensional nonlinear parameter k increases.

For $k = 0.04$, the high power obtained by the nonlinear energy harvesting system appears in the frequency band $\bar{\omega} \in (0.7964, 2)$ than its counterpart part from linear energy harvesting system. And a little high power is harvested in a small frequency band $\bar{\omega} \in (0.5727, 0.5888)$ because of the coexistence of the multiple solutions. The value of the average output power for $k = 0.04$ is smaller than that of for $k = 0.01$ in the non-resonant frequency band $[0.7972, 1.1736]$ and $[1.3515, 2]$. And the similar trends occur for $k = 0.07, 0.1, 0.2, 0.3$ respectively but with two differences that: one is the value of the power becomes smaller as k increases for a fixed nondimensional external frequency during the wider band of $\bar{\omega} \in (0.7964, 2)$, and the other is the new band due to the coexistence of the multiple solutions in the low nondimensional external frequency becomes larger as k increases.

The results indicate that the bandwidth where high power is harvested can be expanded obviously

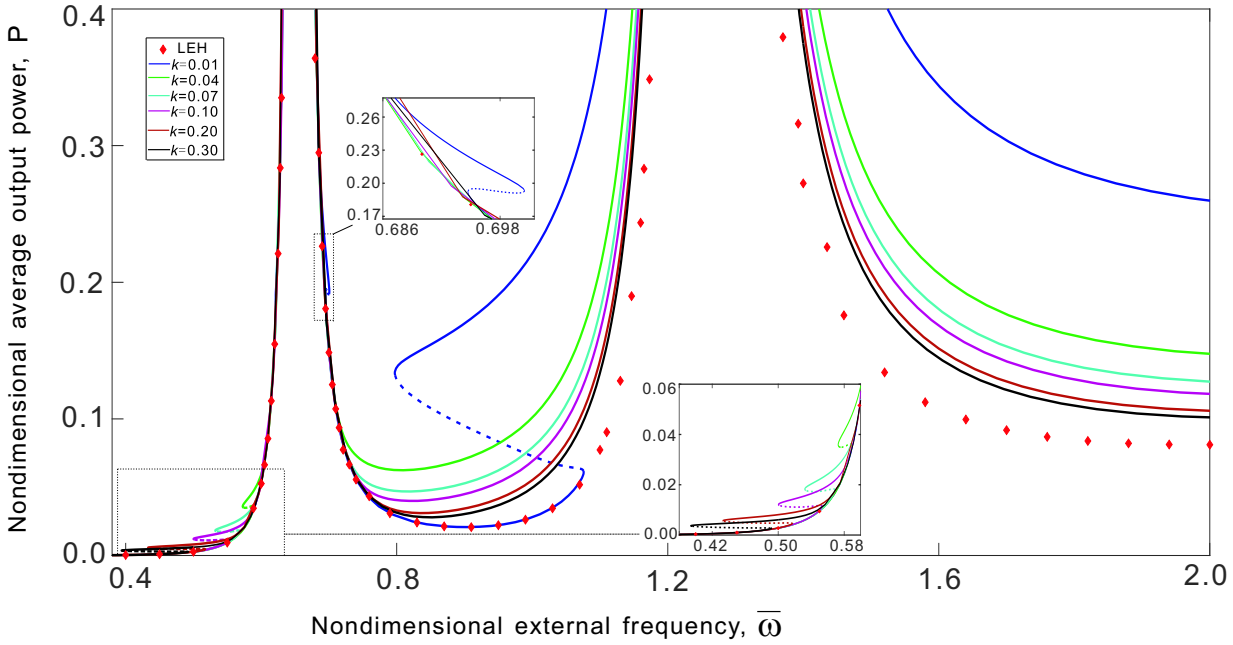

Figure 17: Relation curves of the nondimensional average output power P in terms of the nondimensional external frequency $\bar{\omega}$ with different cubic nonlinear parameter k.

by introducing the nonlinearity and some bands appear by reasons of the coexistence of the multiple solutions.

The effect of the cubic nonlinear parameter k on the average power is investigated as well. As shown in Fig.18 that the values of the power are different when the parameters are selected far from and near the resonant frequency. Fig.18(a) shows that there is a parameter region of k where values of the average power are much larger, such as $k \in (0.0403, 0.2)$ for $\bar{\Omega} = 0.6$, and $k \in (0.0145, 0.0695)$ for $\bar{\Omega} = 0.75$. And in this condition, the larger power would appear in the small nonlinear parameter region when increasing the nondimensional rotating speed. In contrast, the values of the output power are much larger when the parameter selected near the resonant frequency than the other parameter condition, which are mainly related with the frequency. For this reason, the following analysis on the effects of parameters will focus on the parameters selected far from the resonant frequencies.

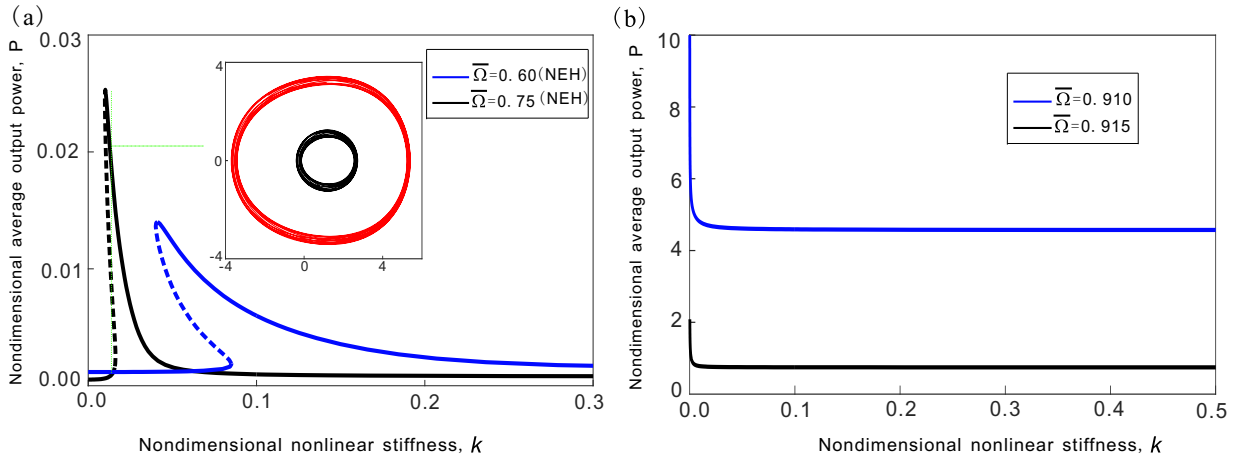

Figure 18: Relation curves of the nondimensional average output power P in terms of the nondimensional cubic nonlinear parameter k with different nondimensional rotating speed: (a) far from the resonance and (b) near the resonance.

The average power from linear and nonlinear energy harvesting system with respect to the nondimensional coupling parameter for the electricalmechanic device η with different nonlinearities is shown in Fig.19. The other parameters are fixed at $\xi = 0.01, \bar{r} = 1, \sigma = 0.1, \bar{\Omega} = 0.75, \bar{\omega} = 0.5$, respectively. As can be seen from Fig.19 that the power displays a linear grow slowly as η increases

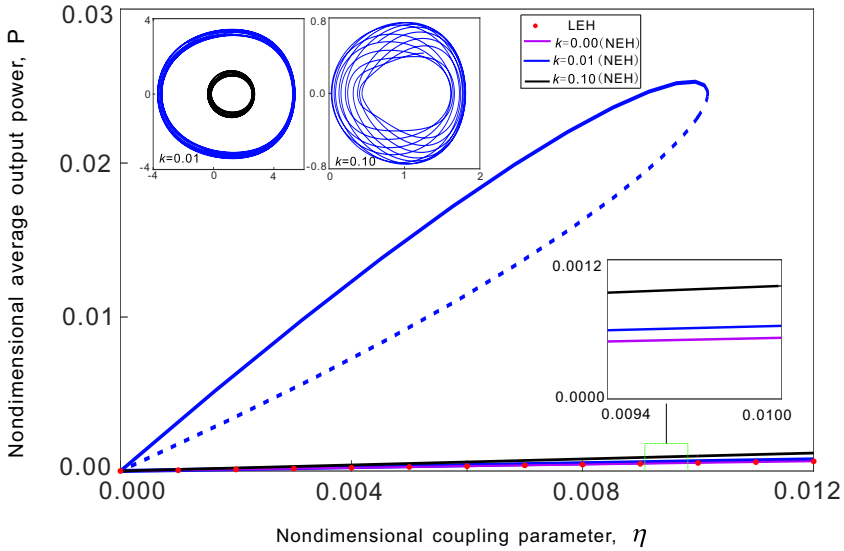

Figure 19: Relation curves of the nondimensional average output power P in terms of the η with different nonlinearities.

when $k = 0$, which has a good agreement for that of linear energy harvester. While for $k = 0.01$, there are two branches of power varying with η increases. One branch for the power has a similar trend but larger value than that of when $k = 0$. The other branch possesses the large value in the wider parameter region $\eta \in (0, 0.0101)$ because of the coexistence of the multiple solutions. In contrast, the value of the average power when $k = 0.1$ is larger than that of the small branch when $k = 0.01$.

In addition, the effects of parameters $\bar{r}, \sigma, k$ on the power harvested from nonlinear system are studied as well, which have no direct relations with the power in the linear energy harvester. Fig.20 shows the relations between the average power from nonlinear energy harvesting with respect to the nondimensional rotating radius $\bar{r}$ with different nonlinearities. There are two types of the response curves of the average power as illustrated in Fig.20: one type with high power appears for the large radius $\bar{r}$, such as $\bar{r} \in (1.8993, 3)$ for $k = 0.005$, and $\bar{r} \in (0.9863, 2.5)$ for $k = 0.01$. While the second type with the high power appears for the small radius $\bar{r}$, such as $\bar{r} \in (0, 1.5)$ for $k = 0.1$, and $\bar{r} \in (0, 1.6)$ for $k = 0.5$. The results indicate that the power harvested from the nonlinear system would become smaller as k increases for a constant rotating radius.

Fig.21 shows the relations between the average power from nonlinear system with respect to the detuning parameter σ for different values of nonlinear parameter k. The other parameters are fixed at $\xi = 0.01, \eta = 0.01, \bar{r} = 1, \bar{\Omega} = 0.75, \bar{\omega} = 0.5$ respectively. As can be seen from Fig.21 that there are two branches of average power in terms of the detuning parameter σ when $k = 0.01$. The band of the parameter region where the effective harvested energy for the small branch reads $\sigma \in (0, 0.0726)$ and the band of the large branch is $\sigma \in (0.0959, 0.2)$. While for $k = 0.03$, there is only one branch of the power which increases quickly from $\sigma = 0.03$ and the value of power is smaller than that of for $k = 0.01$. The results indicate that the nonlinear energy harvesting device could supply a large parameter region for the power harvesting.

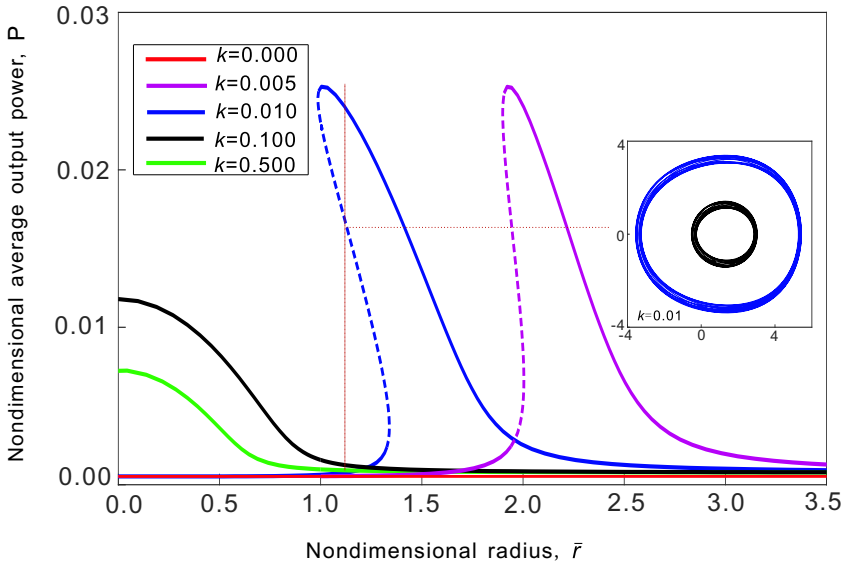

Figure 20: Relation curves of the nondimensional average output power P in terms of the $\bar{r}$ with different nonlinearities

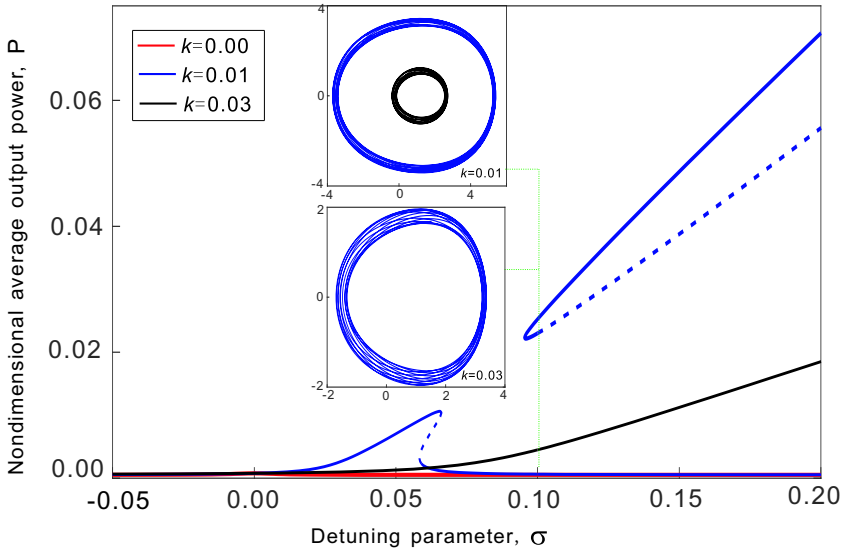

Figure 21: Relation curves of the nondimensional average output power P in terms of the detuning parameter σ with different nonlinearities.

5 Conclusions

A simple nonlinear electromagnetic energy harvester based on a rotating system has been proposed, of which the nonlinear restoring force is derived through the deformation of the horizontal springs. Moreover, some resonant frequency components can be achieved for energy harvesting due to the coupled motions of the base including the rotating and vertical vibrations.

The nonlinear system is modelled and analysed with the method of multiple scale. The dynamic response is studied under the one to one primary resonance condition. The varying trends of the steady-state solutions of the amplitude of the free vibration of the mass in terms of the system parameters including the two external frequencies $\bar{\Omega}$, $\bar{\omega}$, the nonlinear parameter k, the coupling parameter η and the radius $\bar{r}$ are studied. The results show that the magnitude of a can be very large when the external frequencies approach to the resonant frequency, and the saddle-node bifurcation can occur under certain parameter conditions, which indicates the co-existing of the multiple solutions and is verified

by the numerical results. Moreover, for the response of the phase angle ϕ, the main characteristic is the jump phenomenon occurring near the resonant frequencies.

Correspondingly, the varying trends of the average power in terms of different parameters are studied as well. The results illustrate that some main characteristics can occur due to the introduction of the nonlinear restoring force. One aspect is the magnitude of the power, which can be improved during the resonant bands. The second is about the resonant bands which can be extended for different nonlinear parameter k. And the third aspect is about the frequency bands that are induced owing to the nonlinearity of the system, during which the average power is much larger than that of for the linear system. In addition, the relations for the average power and the other parameters including the nondimensional radius $\bar{r}$, the detuning parameter σ, the nondimensional electromechanical coupling coefficient η are also investigated. For the corresponding linear system, the power has less relations with these parameters. But for the nonlinear system, the results indicate that some wider parameter regions can occur for large-value power harvesting. This design can be used to transfer the vibration energy of some rotating devices to the electrical power for some mini-type monitoring devices. The experimental study will be followed in the further work.

Acknowledgement

The authors acknowledge the financial supports of the National Natural Science Foundation of China (No.11702111, 11732014,11872201, 12172166) and the State Scholarship Fund of CSC.

Declarations

The authors declare that they have no conflict of interest.

References

[1] Beeby, S. P., Tudor, M. J., White, N. Energy harvesting vibration sources for microsystems applications. Measurement Science and Technology, 2006, 17(12): R175.

[2] Deng L., Fang Y., Wang D., Wen Z. A MEMS based piezoelectric vibration energy harvester for fault monitoring system. Microsystem Technologies, 2018, 24: 3637-3644.

[3] Wei C., Jing X. A comprehensive review on vibration energy harvesting: Modelling and realization. Renewable and Sustainable Energy Reviews, 2017, 74: 1-18.

[4] Foong F. M., Thein C. K., Ooi B. L., Yurchenko D. Increased power output of an electromagnetic vibration energy harvester through anti-phase resonance. Mechanical Systems and Signal Processing, 2019, 116: 129-145.

[5] Zhou K., Dai H. L., Abdelkefic A., Ni Q. Theoretical modeling and nonlinear analysis of piezoelectric energy harvesters with different stoppers. International Journal of Mechanical Sciences, 2020, 166: 105233.

[6] Rui X., Zeng Z., Li Y., Zhang Y., Yang Z., Huang X., Sha Z. Modeling and analysis of a rotational piezoelectric energy harvester with limiters. Journal of Mechanical Science and Technology, 2019, 33(11): 5169-5176.

[7] Owens B. A. M., Mann B. P. Linear and nonlinear electromagnetic coupling models in vibration-based energy harvesting. Journal of Sound and Vibration, 2012, 331: 922-937.

[8] Firoozy P., Khadem S. E., Pourkiaee S. M. Power enhancement of broadband piezoelectric energy harvesting using a proof mass and nonlinearities in curvature and inertia. International Journal of Mechanical Sciences, 2017, 133: 227-239.

[9] Rubes O., Brablc M., Hadas Z. Nonlinear vibration energy harvester: Design and oscillating stability analyses. Mechanical Systems and Signal Processing, 2019, 125: 170-184.

[10] Kecik K., Borowiec M. An auto parametric energy harvester. The European Physical Journal Special Topics, 2013, 222: 1597-1605.

[11] Halvorsen E. Fundamental issues in nonlinear wide band-vibration energy harvesting. Physical Review E, 2013, 87: 042129.

[12] Yang L. J., Zhang H. F. Experimental study on a wide-band piezoelectric energy harvester with rotating beams vibrating in perpendicular directions. Integrated Ferroelectrics, 2016, 168(1): 85-96.

[13] Xu M., Jin X., Wang Y., Huang Z. Stochastic averaging for nonlinear vibration energy harvesting system. Nonlinear Dynamics, 2014, 78: 1451-1459.

[14] Harne R. L., Wang K. W. Axial suspension compliance and compression for enhancing performance of a nonlinear vibration energy harvesting beam system. ASME-Journal of Vibration and Acoustics, 2016, 138-011004-1.

[15] Thomson G., Lai Z., Val D.V., Yurchenko D. Advantages of nonlinear energy harvesting with dielectric elastomers. Journal of Sound and Vibration, 2019, 442: 167-182.

[16] Yildirim T., Ghayesh M. H., Li W., Alici G. A review on performance enhancement techniques for ambient vibration energy harvesters. Renewable and Sustainable Energy Reviews. 2017, 71: 435-449.

[17] Akcabay D. T., Young. Y. L. Scaling the dynamic response and energy harvesting potential of piezoelectric beams. Applied Physics Letters, 2012, 101: 264104.

[18] Cottone F., Gammaitoni L., Vocca H., Ferrari M., Ferrari V. Piezoelectric buckled beams for random vibration energy harvesting. Smart Materials and Structures, 2012, 21, 035021.

[19] Alevras P., Theodossiades S., Rahnejat H. On the dynamics of a nonlinear energy harvester with multiple resonant zones. Nonlinear Dynamics, 2018, 92: 1271-1286.

[20] Mann B. P., Sims N. D. Energy harvesting from the nonlinear oscillations of magnetic levitation. Journal of Sound and Vibration, 2009, 319: 515-530.

[21] Tai W. C., Liu M., Yuan Y., Zuo L. On improvement of the frequency bandwidth of nonlinear vibration energy harvesters using a mechanical motion rectifier. Journal of Vibration and Acoustics, 2018, 140/051008,1-11.

[22] Shan G., Wang D. F., Song J., Fu Y., Yang X. A spring-assisted adaptive bistable energy harvester for high output in low-excitation. Microsystem Technologies, 2018, 24, 3579-3588.

[23] Lai S., Wang C., Zhang L. A nonlinear multi-stable piezomagnetoelastic harvester array for low-intensity, low-frequency, and broadband vibrations. Mechanical Systems and Signal Processing, 2019, 122: 87-102.

[24] Jiang W. A., Chen L. Q. An equivalent linearization technique for nonlinear piezoelectric energy harvesters under Gaussian white noise. Communications in Nonlinear Science and Numerical Simulation, 2014, 19: 2897-2904.

[25] Awrejcewicz J., Starosta R., Sypniewska-Kamińska G. Nonlinear vibration of a lumped system with springs-in-series. Meccanica, 2020, 1-15.

[26] Kudra G., Witkowski K., Rezaei M. P., Awrejcewicz J. Mathematical modelling and experimental validation of bifurcation dynamics of one-degree-of-freedom oscillator with Duffing-type stiffness and rigid obstacle. Journal of Vibration Engineering and Technologies, 2023, 1-8.

[27] Zhou S. X., Zuo L. Nonlinear dynamic analysis of asymmetric tristable energy harvesters for enhanced energy harvesting. Communications in Nonlinear Science and Numerical Simulation, 2018, 61, 271-284.

[28] Wang X., Wu H., Yang B. Nonlinear multi-modal energy harvester and vibration absorber using magnetic softening spring. Journal of Sound and Vibration, 2020, 476: 115332.

[29] Cao Q. J., Wiercigroch M., Pavlovskaia E. E. An archetypal oscillator for smooth and discontinuous dynamics. Physical Review E, 2006, 74: 046218.

[30] Hao Z. F., Cao Q. J., Wiercigroch M. Nonlinear dynamics of the quasi-zero-stiffness SD oscillator based upon the local and global bifurcation analyses. Nonlinear Dynamics, 2017, 87: 987-1014.

[31] Harne R. L., Wang K. W. Topical Review: A review of the recent research on vibration energy harvesting via bistable Systems. Smart Materials and Structures, 2013, 22, 023001, 1-12.

[32] McCarthy J. M., Watkins S., Deivasigamani A., John S. J. Fluttering energy harvesters in the wind: A review. Journal of Sound and Vibration, 2016, 361: 355-377.

[33] Zhang J., Fang Z., Shu C., Zhang J., Zhang Q., Li C. A rotational piezoelectric energy harvester for efficient wind energy harvesting. Sensors and Actuators A: Physical, 2017, 262: 123-129.

[34] Seo J., Jhang K. Y., Lee H., Kim Y. C. Vibration energy harvesting technology for smart tire monitoring. Journal of Mechanical Science and Technology, 2019, 33(8): 3725-3732.

[35] Micek P., Grzybek D. Wireless stress sensor based on piezoelectric energy harvesting for a rotating shaft. Sensors and Actuators A: Physical, 2020, 301, 111744.

[36] Pillatsch P., Yeatman E. M., Holmes A. S. A piezoelectric frequency up-converting energy harvester with rotating proof mass for human body applications. Sensors and Actuators A, 2014, 206: 178-185.

[37] Halim M.A., Rantz R., Zhang Q., Gu L., Yang K., Roundy S. An electromagnetic rotational energy harvester using sprung eccentric rotor, driven by pseudo-walking motion. Applied Energy, 2018, 217: 66-74.

[38] Fu H., Yeatman E. M. A methodology for low-speed broadband rotational energy harvesting using piezoelectric transduction and frequency up-conversion. Energy, 2017, 125: 152-161.

[39] Clifford M. J., Bishop S. R. Rotating periodic orbits of the parametrically excited pendulum. Physics Letters A, 1995, 201: 191-196.

[40] Nandakumar K., Wiercigroch M., Chatterjee A. Optimum energy extraction from rotational motion in a parametrically excited pendulum. Mechanics Research Communications, 2012, 43, 7-14.

[41] Najdecka A., Narayanan S., Wiercigroch M. Rotary motion of the parametric and planar pendulum under stochastic wave excitation. International Journal of Non-Linear Mechanics, 2015, 71: 30-38.

[42] Gonz*á*lez A. T., Dunning P., Howard I., McKee K., Wiercigroch M. Is wave energy untapped potential? International Journal of Mechanical Sciences, 2021, 205, 106544.

[43] Abohamer M. K., Awrejcewicz J., Starosta R., Amer T. S., Bek M. A. Influence of the motion of a spring pendulum on energy-harvesting devices. Applied Sciences, 2021, 11, 8658.

[44] Sypniewska-Kami*ń*ska G., Starosta R., Awrejcewicz J. Quantifying nonlinear dynamics of a spring pendulum with two springs in series: an analytical approach. Nonlinear Dynamics, (2022) 110: 1-36.

[45] Kecik K. Simultaneous vibration mitigation and energy harvesting from a pendulum-type absorber. Communications in Nonlinear Science and Numerical Simulations, 2021, 92: 105479.

[46] Toh T. T., Mitcheson P. D., Holmes A. S., Yeatman E. M. (2008) A continuously rotating energy harvester with maximum power point tracking. Journal of Micromechanics and Microengineering, 2008, 18: 104008, 1-7.

[47] Yeatman, E. M. Energy harvesting from motion using rotating and gyroscopic proof masses. Proceedings of the Institution of Mechanical Engineers, Part C: Journal of Mechanical Engineering Science, 2008, 222(1): 27-36.

[48] Trimble, A. Z., Lang, J. H., Pabon, J., and Slocum, A. A device for harvesting energy from rotational vibrations. ASME Journal of Mechanical Design, 2010, 132(9): 091001.

[49] Ramezanpour R., Nahvi H., Ziaei-Rad S. A vibration-based energy harvester suitable for low-frequency, high amplitude environments: Theoretical and experimental investigations. Journal of Intelligent Material Systems and Structures, 2016, 27(5), 642-665.

[50] Häggström F., Gustafsson J., Delsing J. Energy harvesting technologies for wireless sensors in rotating environments. Proceedings of the 2014 IEEE Emerging Technology and Factory Automation (ETFA), Barcelona, 2014, 1-4.

[51] Xie Z., Xiong J., Zhang D., Wang T., Shao Y., Huang W. Design and experimental investigation of a piezoelectric rotation energy harvester using bistable and frequency up-conversion mechanisms. Applied Sciences, 2018, 8: 1418.

[52] Zhang Y., Zheng R., Nakano K., Cartmell M. P. Stabilising high energy orbit oscillations by the utilisation of centrifugal effects for rotating-tyre-induced energy harvesting. Applied Physics Letters, 2018, 112: 143901.

[53] Liu Z., Wang X., Ding S., Zhang R., McNabb L. A new concept of speed amplified nonlinear electromagnetic vibration energy harvester through fixed pulley wheel mechanisms and magnetic springs. Mechanical Systems and Signal Processing, 2019, 126: 305-325.

[54] Chen Y., Yan Z. Nonlinear analysis of axially loaded piezoelectric energy harvesters with flexoelectricity. International Journal of Mechanical Sciences, 2020, 173: 105473, 1-11.

[55] Cooley C. G., Chai T. Energy harvesting from the vibrations of rotating systems. Journal of Vibration and Acoustics, 2018, 140: 021010, 1-11.

[56] Wang J., Liao W. H. Attaining the high-energy orbit of nonlinear energy harvesters by load perturbation. Energy Conversion and Management, 2019, 192: 30-36.

[57] Zhang Y., Zheng R., Shimono K., Kaizuka T., Nakano K. Effectiveness testing of a piezoelectric energy harvester for an automobile wheel using stochastic resonance. Sensors, 2016, 16: 1727.

[58] Kim H., Tai W. C., Parker J., Zuo L. Self-tuning stochastic resonance energy harvesting for rotating systems under modulated noise and its application to smart tires. Mechanical Systems and Signal Processing, 2019, 122: 769-785.

[59] Alevras P., Theodossiades S. Vibration energy harvester for variable speed rotor applications using passively self-tuned beams. Journal of Sound and Vibration, 2019, 444, 176-196.

[60] Gu L., Livermore C. Compact passively self-tuning energy harvesting for rotating applications. Smart Materials and Structures, 2012, 21: 015002

[61] Dai Q., Harne R. L. Charging power optimization for nonlinear vibration energy harvesting systems subjected to arbitrary, persistent base Excitations. Smart Materials and Structures, 2018, 27: 015011

[62] Lu H., Chai T., Cooley C. G. Vibration properties of a rotating piezoelectric energy harvesting device that experiences gyroscopic effects. Journal of Sound and Vibration, 2018, 416: 258-278.

[63] Roundy S., Tola J. Energy harvester for rotating environments using offset pendulum and nonlinear dynamics. Smart Materials and Structures, 2014, 23(10), 105004.

[64] Guan M., Liao W. H. Design and analysis of a piezoelectric energy harvester for rotational motion system. Energy Conversion and Management, 2016, 111, 239-244.

[65] Febboa M., Machadob S. P., Gattib C. D., Ramirez J. M. An out-of-plane rotational energy harvesting system for low frequency environments. Energy Conversion and Management, 2017, 152: 166-175.

[66] Williams C. B., Yates R. B. Analysis of a micro-electric generator for microsystems. Sensors and Actuators A, 1996, 52: 8-11.

[67] Hao Z. F., Cao Q. J., Wiercigroch M. Two-sided damping constraint control for high-performance vibration isolation and end-stop impact protection. Nonlinear Dynamics, 2016, 86: 2129-2144.

[68] Wang D., Chen Y. S., Wiercigroch M., Cao Q. J. Bifurcation and dynamic response analysis of rotating blade excited by upstream vortices. Applied Mathematics and Mechanics, 2016, 37(9): 1251-1274.

[69] Nayfeh A.H., Mook D.T. *Nonlinear oscillations*. 1979, New York.

[70] Amer W.S., Amer T.S., Starosta R., Bek M.A. Resonance in the Cart-Pendulum SystemłAn Asymptotic Approach. Applied Sciences, 2021, 11, 11567. https://doi.org/10.3390/app112311567

[71] Awrejcewicz J., Starosta R., Sypniewska-Kamińska G. Asymptotic Multiple Scale Method in Time Domain-*Multi-Degree-of-Freedom Stationary and Nonstationary Dynamics*. 2022, CRC Press